

**AFRL-PR-WP-TR-2003-2052**

**THERMAL MANAGEMENT  
RESEARCH FOR POWER  
GENERATION**

**Delivery Order 0002 - Volume 2: Closed-Loop  
Spray Cooling of High-Power Semiconductor  
Lasers**



**Lanchao Lin, Ph.D.**

**UES, Inc  
4401 Dayton-Xenia Road  
Dayton, OH 45432-1894**

**DECEMBER 2002**

**Final Report for 01 April 2000 – 30 October 2002**

**Approved for public release; distribution is unlimited.**

**PROPULSION DIRECTORATE  
AIR FORCE RESEARCH LABORATORY  
AIR FORCE MATERIEL COMMAND  
WRIGHT-PATTERSON AIR FORCE BASE, OH 45433-7251**

## NOTICE

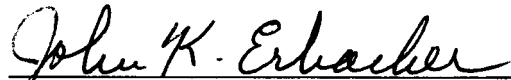
USING GOVERNMENT DRAWINGS, SPECIFICATIONS, OR OTHER DATA INCLUDED IN THIS DOCUMENT FOR ANY PURPOSE OTHER THAN GOVERNMENT PROCUREMENT DOES NOT IN ANY WAY OBLIGATE THE US GOVERNMENT. THE FACT THAT THE GOVERNMENT FORMULATED OR SUPPLIED THE DRAWINGS, SPECIFICATIONS, OR OTHER DATA DOES NOT LICENSE THE HOLDER OR ANY OTHER PERSON OR CORPORATION; OR CONVEY ANY RIGHTS OR PERMISSION TO MANUFACTURE, USE, OR SELL ANY PATENTED INVENTION THAT MAY RELATE TO THEM.

THIS REPORT IS RELEASABLE TO THE NATIONAL TECHNICAL INFORMATION SERVICE (NTIS). AT NTIS, IT WILL BE AVAILABLE TO THE GENERAL PUBLIC, INCLUDING FOREIGN NATIONS.

THIS TECHNICAL REPORT HAS BEEN REVIEWED AND IS APPROVED FOR PUBLICATION.



RENGASAMY PONNAPPAN  
Senior Mechanical Engineer  
Energy Storage & Thermal Sciences Branch



JOHN K. ERBACHER  
Acting Branch Chief  
Energy Storage & Thermal Sciences Branch



C. SCOTT RUBERTUS  
Acting Deputy Chief  
Power Division

Do not return copies of this report unless contractual obligations or notice on a specific document requires its return.

<b>REPORT DOCUMENTATION PAGE</b>					Form Approved OMB No. 0704-0188				
The public reporting burden for this collection of information is estimated to average 1 hour per response, including the time for reviewing instructions, searching existing data sources, gathering and maintaining the data needed, and completing and reviewing the collection of information. Send comments regarding this burden estimate or any other aspect of this collection of information, including suggestions for reducing this burden, to Department of Defense, Washington Headquarters Services, Directorate for Information Operations and Reports (0704-0188), 1215 Jefferson Davis Highway, Suite 1204, Arlington, VA 22202-4302. Respondents should be aware that notwithstanding any other provision of law, no person shall be subject to any penalty for failing to comply with a collection of information if it does not display a currently valid OMB control number. <b>PLEASE DO NOT RETURN YOUR FORM TO THE ABOVE ADDRESS.</b>									
<b>1. REPORT DATE (DD-MM-YY)</b> December 2002		<b>2. REPORT TYPE</b> Final		<b>3. DATES COVERED (From - To)</b> 04/01/2000 – 10/30/2002					
<b>4. TITLE AND SUBTITLE</b> THERMAL MANAGEMENT RESEARCH FOR POWER GENERATION Delivery Order 0002 - Volume 2: Closed-Loop Spray Cooling of High-Power Semiconductor Lasers				<b>5a. CONTRACT NUMBER</b> F33615-98-D-2867					
				<b>5b. GRANT NUMBER</b>					
				<b>5c. PROGRAM ELEMENT NUMBER</b> 62203F					
<b>6. AUTHOR(S)</b> Lanchao Lin, Ph.D.				<b>5d. PROJECT NUMBER</b> 3145					
				<b>5e. TASK NUMBER</b> 32					
				<b>5f. WORK UNIT NUMBER</b> Z3					
<b>7. PERFORMING ORGANIZATION NAME(S) AND ADDRESS(ES)</b> UES, Inc 4401 Dayton-Xenia Road Dayton, OH 45432-1894				<b>8. PERFORMING ORGANIZATION REPORT NUMBER</b> UES-P183-03-601					
<b>9. SPONSORING/MONITORING AGENCY NAME(S) AND ADDRESS(ES)</b> Propulsion Directorate Air Force Research Laboratory Air Force Materiel Command Wright-Patterson Air Force Base, OH 45433-7251				<b>10. SPONSORING/MONITORING AGENCY ACRONYM(S)</b> AFRL/PRPS					
				<b>11. SPONSORING/MONITORING AGENCY REPORT NUMBER(S)</b> AFRL-PR-WP-TR-2003-2052					
<b>12. DISTRIBUTION/AVAILABILITY STATEMENT</b> Approved for public release; distribution is unlimited.									
<b>13. SUPPLEMENTARY NOTES</b> Report contains color. See also AFRL-PR-WP-TR-2003-2051, Volume 1: Plain Fin Array Cooler for Electronics Cooling.									
<b>14. ABSTRACT</b> A closed-loop spray cooling test setup is established for the cooling of high-power diode lasers. Eight miniature nozzles in a multinozzle plate are used to generated a spray array targeting at a 1 by 2 cm <sup>2</sup> cooling surface. FC-87, FC-72, methanol, and water are used as the working fluids. Thermal performance data for the multinozzle spray cooling in the confined and closed system are obtained at various operating temperatures, nozzle pressure drops (from 0.69 bar to 3.10 bar), and heat fluxes. It is demonstrated that the spray cooler can reach the critical heat fluxes up to 90 W/cm <sup>2</sup> with fluorocarbon fluids and 490 W/cm <sup>2</sup> with methanol. For water, the critical heat flux is higher than 500 W/cm <sup>2</sup> . It is found that air purposely introduced in the spray cooling system with FC-72 fluid has a significant influence on heat transfer characteristics of the spray over the cooling surface. A semiempirical correlation of CHF is presented using the present experimental data for the multinozzle spray cooling in the confined and closed system without air.									
<b>15. SUBJECT TERMS</b> diode laser, high power semiconductor laser, spray cooling, heat transfer enhancement, critical heat flux, closed loop, two-phase flow									
<b>16. SECURITY CLASSIFICATION OF:</b> <table border="1" style="width: 100%; border-collapse: collapse; margin-top: 5px;"> <tr> <td style="padding: 2px;"><b>a. REPORT</b> Unclassified</td> <td style="padding: 2px;"><b>b. ABSTRACT</b> Unclassified</td> <td style="padding: 2px;"><b>c. THIS PAGE</b> Unclassified</td> </tr> </table>			<b>a. REPORT</b> Unclassified	<b>b. ABSTRACT</b> Unclassified	<b>c. THIS PAGE</b> Unclassified	<b>17. LIMITATION OF ABSTRACT:</b> SAR		<b>18. NUMBER OF PAGES</b> 70	
<b>a. REPORT</b> Unclassified	<b>b. ABSTRACT</b> Unclassified	<b>c. THIS PAGE</b> Unclassified							
<b>19a. NAME OF RESPONSIBLE PERSON (Monitor)</b> Rengasamy Ponnappan					<b>19b. TELEPHONE NUMBER (Include Area Code)</b> (937) 255-2922				

## TABLE OF CONTENTS

	<b>Page</b>
<b>LIST OF FIGURES</b>	v
<b>LIST OF TABLES</b>	viii
<b>NOMENCLATURE</b>	ix
<b>FOREWORD</b>	xi
<b>1 INTRODUCTION</b>	1
<b>1.1 Current and Temperature of Diode Lasers</b>	2
<b>1.2 Thermal Management of High Power Diode Laser Array</b>	6
<b>1.3 Scope of the Present Research</b>	9
<b>2 MULTI-NOZZLE ASSEMBLY DEVELOPMENT</b>	10
<b>2.1 Multi-nozzle Assembly Design</b>	10
<b>2.2 Multi-nozzle Spray Characteristics in the Atmosphere</b>	13
<b>3 EXPERIMENTAL SETUP AND PROCEDURE</b>	16
<b>3.1 Thermal Performance Test Setup</b>	16
<b>3.2 Visualization Setup</b>	22
<b>3.3 Measurement Uncertainty</b>	24
<b>4 RESULTS AND DISCUSSION</b>	25
<b>4.1 Spray Cooling Pattern in Confined Chamber</b>	25
<b>4.2 Heat Transfer Characteristics</b>	26
<b>4.3 Critical Heat Flux</b>	36
<b>4.4 Effect of Noncondensable Gas</b>	38
<b>5 CRITICAL HEAT FLUX CORRELATION</b>	42
<b>6 CONCLUSIONS AND RECOMMENDATIONS</b>	46
<b>6.1 Conclusions</b>	46
<b>6.2 Recommendations</b>	47
<b>7 REFERENCES</b>	48

<b>APPENDIX A: WORKING FLUID PROPERTIES</b>	51
<b>APPENDIX B: MEAN DIAMETERS</b>	53

## LIST OF FIGURES

Figure	Page
1.1 Light output of a semiconductor diode laser above and below laser threshold current.	4
1.2 L-I curve of a quasi-cw laser array bar emitting near 807 nm wavelength, showing a conversion efficiency above 50%.	5
1.3 Assembly of diode laser bars in connection with heat sink.	7
1.4 Stacking the diode laser bars.	7
2.1 Multi-nozzle assembly.	10
2.2 Swirler insert.	11
2.3 Multi-nozzle plate.	11
2.4 Water spray pattern of a desired nozzle at a 2.76 bar pressure drop.	13
2.5 Eight-nozzle spray pattern with FC-72 as the working fluid at the pressure drop of 2.76 bar.	14
2.6 Relation between liquid flow rate and pressure drop across the eight nozzles for the spray into the atmospheric environment.	15
3.1 Photographic view of the test setup.	17
3.2 Schematic of test setup.	18
3.3 Insulation plate.	20
3.4 Heater plate with thermocouple holes	21
3.5 Photographic view of the visualization setup.	23
4.1 Spray cooling pattern.	25
4.2 Effect of volumetric flux on heat transfer characteristics for FC-87 at $T_{\text{sat}}=42^{\circ}\text{C}$ .	27
4.3 Effect of volumetric flux on heat transfer characteristics for FC-87 at $T_{\text{sat}}=32^{\circ}\text{C}$ .	27
4.4 Effect of volumetric flux on heat transfer characteristics for FC-87 at $T_{\text{sat}}=22^{\circ}\text{C}$ .	28
4.5 Effect of spray saturation temperature on heat transfer characteristics for FC-87 at $\Delta p=1.03$ bar.	28

## LIST OF FIGURES (CONT'D.)

Figure	Page
4.6 Effect of volumetric flux on heat transfer characteristics for FC-72 at $T_{\text{sat}}=53^{\circ}\text{C}$ .	29
4.7 Effect of volumetric flux on heat transfer characteristics for FC-72 at $T_{\text{sat}}=36^{\circ}\text{C}$ .	29
4.8 Effect of spray saturation temperature on heat transfer characteristics for FC-72 at $\Delta p=1.72$ bar.	30
4.9 Effect of volumetric flux on heat transfer characteristics for methanol at $T_{\text{sat}}=66.6^{\circ}\text{C}$ to $69.0^{\circ}\text{C}$ .	31
4.10 Effect of volumetric flux on heat transfer characteristics for methanol at $T_{\text{sat}}=50.3^{\circ}\text{C}$ to $53.7^{\circ}\text{C}$ .	32
4.11 Effect of spray saturation temperature on heat transfer characteristics for methanol at $\Delta p=1.72$ bar.	32
4.12 Effect of volumetric flux on heat transfer characteristics for water at $T_{\text{sat}}=80.5^{\circ}\text{C}$ to $84.3^{\circ}\text{C}$ .	33
4.13 Effect of volumetric flux on heat transfer characteristics for water at $T_{\text{sat}}=67^{\circ}\text{C}$ to $72^{\circ}\text{C}$ .	34
4.14 Effect of spray saturation temperature on heat transfer characteristics for water at $\Delta p=1.72$ bar.	34
4.15 CHF vs. $Q''$ at different saturation temperature levels for FC-87.	37
4.16 CHF vs. $Q''$ at different saturation temperature levels for FC-72.	37
4.17 CHF vs. $Q''$ at different saturation temperature levels for methanol.	38
4.18 Effect of noncondensable gas on the relation between heat flux and hot surface temperature.	39
4.19 Effect of noncondensable gas on heat transfer characteristics over the hot surface.	40
4.20 Comparison of CHF data for pure FC-72 and FC-72 with air.	41

## LIST OF FIGURES (CONT'D.)

Figure	Page
5.1 Vapor and liquid interaction near CHF.	42
5.2 Comparison of data with CHF correlation.	45



## LIST OF TABLES

<b>Table</b>	<b>Page</b>
2.1 Nozzle geometric parameters.	12
4.1 Spray cooling parameters.	36
B.1 Mean diameters and their applications.	53

## NOMENCLATURE

$a_1$	constant
$a_2$	constant
$A_v$	cross-sectional area of vapor stem, $m^2$
$A_w$	area of hot surface, $m^2$
$b$	critical liquid disc thickness, m
$c$	constant
$c_w$	constant
$d_d$	liquid disc diameter, m
$d_o$	nozzle orifice diameter, m
$d_{20}$	surface mean diameter of spray, m
$d_{32}$	Sauter mean diameter (SMD), m
$h_{fg}$	latent heat of vaporization, J/kg
$h$	heat transfer coefficient, $W/m^2K$
$I$	current, A
$I_{th}$	threshold current, A
$k_h$	thermal conductivity of heater plate, $W/mK$
$N$	rate of droplets impinging per unit area, $/m^2 \cdot s$
$p_1$	pressure at the outlet of condenser, Pa
$p_2$	pressure at the inlet of liquid chamber, Pa
$p_3$	spray chamber pressure, Pa
$P$	light output power, W
$q''$	heat flux (heat rate per unit cooling area), $W/cm^2$
$q''_c$	critical heat flux, $W/cm^2$
$Q''$	volumetric flow rate per unit cooling area, $m^3/m^2 \cdot s$
$T$	temperature, $^{\circ}C$
$T_b$	boiling point, $^{\circ}C$
$T_{ch}$	spray chamber temperature, $^{\circ}C$

$T_{\text{ch,o}}$	spray chamber outlet temperature, °C
$u_v$	vapor velocity, m/s
We	spray Weber number, $r_l Q^{1/2} d_{32} / \sigma$
$\beta$	spreading ratio, $d_d / d_{20}$
$\Delta p$	pressure drop across spray nozzle, Pa
$\eta_c$	effectiveness of spray cooling at CHF
$\eta_D$	differential quantum efficiency
$\vartheta$	swirl chamber cone angle, °
$\lambda$	lasing wavelength, nm
$\lambda_H$	Helmholtz critical wavelength, m
$\mu_l$	liquid dynamic viscosity, N·s/m <sup>2</sup>
$\rho$	density, kg/m <sup>3</sup>
$\sigma$	surface tension, N/m

### Subscripts

l	liquid
m	mean value
sat	saturation
v	vapor
w	cooling surface

## **FOREWORD**

This final technical report is part of the contract deliverables under the contract F33615-98-D-2867/Delivery Order #0002 titled "Thermal Management Research for Power Generation". This contract was sponsored and administered by Propulsion Directorate (PR) of Air Force Research Laboratory (AFRL), Wright-Patterson Air Force Base. The present report deals with closed loop spray cooling of high power semiconductor lasers. The research effort was performed under Task 1, Laser Diode Cooling. Dr. Rengasamy Ponnappan (AFRL/PRPS) was the Air Force Senior Mechanical Engineer/Technical Monitor for this program.

The work presented here was carried out at the Power Division's Thermal Laboratory by UES, Inc., Dayton, Ohio, with Dr. Lanchao Lin as the Principal Investigator. Roger P. Carr and John E. Tennant (UES, Inc.) provided the technical support. UES's Materials and Processes Division and contract office provided the administrative support. The author wishes to thank Richard J. Harris, University of Dayton Research Institute, for his efforts in designing and fabricating the nozzle array and establishing the data acquisition system.

# 1 INTRODUCTION

Spray cooling as the high heat flux removal technique has potentials for high power systems. The spray cooling with phase change takes advantage of relatively large amounts of latent heat and is capable of removing high heat fluxes from surfaces with low superheat. With water as the working fluid, a spray cooling heat flux of  $1000\text{W}/\text{cm}^2$  has been demonstrated [1]. Recent applications of spray cooling involved the cooling of different kinds of electronics. In the application, a major portion of heat transfer results from nucleate boiling heat transfer. Other emerging applications include the cooling of high power directed energy sources operating in the space environment and generating heat at heat flux levels greater than  $500\text{ W}/\text{cm}^2$ .

Several experiments were performed by many researchers in order to understand nucleate boiling heat transfer and critical heat flux (CHF) for full cone sprays using single nozzles [1-6] and multiple nozzles [7]. The effects of spray nozzle, volumetric flux, Sauter mean diameter of spray, subcooling and working fluid were investigated. The heat transfer mechanism of spray cooling is associated with phenomena such as nucleate boiling due to surface nucleation and secondary nucleation, convection heat transfer, and direct evaporation from the surface of liquid film [2]. The concept of secondary nucleation is helpful for understanding the heat transfer enhancement of spray cooling. It has been concluded that increasing the droplet flux increases the number of secondary nuclei, increases heat transfer of nucleate boiling and convection, and helps to lower surface temperature for a given heat flux [2].

Mudawar and Valentine conducted an experimental study of spray cooling to determine local quenching characteristics for various regimes of a water spray boiling curve [3]. It was found that the volumetric flux had a dominant effect on heat transfer compared to other hydrodynamic properties of the spray [3]. Sehmbe et al. investigated the effect of surface material properties and surface characteristics on spray cooling heat transfer using air atomized nozzles [4]. A higher contact angle showed an enhanced heat transfer due to the ease in nucleation and a smooth surface ( $0.3\text{ }\mu\text{m}$  polish) showed a dramatic increase in heat flux due to the thinner liquid film [4]. Yang et al. presented a heat transfer correlation based on water spray data in the nucleate boiling regime [1]. In their experiment, an air atomized nozzle was used. Estes and Mudawar presented a CHF correlation with suitable dimensionless parameters that accurately predicted data for FC-72, FC-87 and water [5]. The

correlation by Estes and Mudawar had a strong dependence of CHF on volumetric flux and Sauter mean diameter. Sehmbe et al. developed a semiempirical correlation for CHF that was based on macrolayer dryout model and correlated with data for water and LN2 [6]. Lin and Ponnappan investigated CHF of multi-nozzle spray cooling in a closed loop and obtained a CHF correlation using their experimental data [7].

Most available spray cooling data were related with the free spray cooling in a large space or the spray cooling of small surfaces using a single nozzle. In most experiments, the applied pressure drops across the nozzle were greater than 2.0 bar [3-6] and there existed air, more or less, in the spray cooling systems [1-6]. The present investigation deals with multi-nozzle spray cooling in the confined spray chamber and the flow is circulated within a closed loop. The test setup is established to simulate the cooling of high power diode laser arrays (DLAs). The use of spray cooling technology in this application is to ensure a minimum temperature gradient between emitters and along the cavity length of the emitter. A multi-nozzle plate embedded with eight miniature nozzles is used. The target spray cooling area is  $1 \times 2 \text{ cm}^2$  and the design is scaleable to large cooling areas for DLA application. The applied pressure drops across the nozzle range from 0.69 bar to 3.1 bar. To maintain the optimum thermal performance of the closed loop spray cooling system, the system is evacuated before filling a proper amount of the working fluid. Heat transfer characteristics and CHF of the closed loop spray cooling system are presented. The effect of the noncondensable gas on the thermal performance of the spray cooling is described.

## **1.1 Current and Temperature of Diode Lasers**

During the last ten years, high-power edge-emitting diode lasers have developed rapidly both in optical output and in lifetime. The typical output from a single commercially available diode laser bar jumped from 20 to 50 W continuous wave (CW) by 1999 [8] and to 100 W by 2001 [9]. Typical expected lifetimes increased from 1000 to 10,000 h. This amounts to a factor of 50 performance increase for commercially available high power diode lasers. Within a few years, 200 W bars will be commercially available. Most applications of the diode lasers involve pumping of solid-state lasers and direct use in the field of medicine. In application to the pumping of solid-state lasers (e.g, YAG lasers), the wavelength of the diode laser array (GaAlAs) should be well-tuned to the absorption

spectrum of the YAG crystal (806-810 nm).

The advanced technology of micro electromechanical systems (MEMS) allows users to combine large groups of diode lasers to create stacks. Stacking individual diode laser submounts after collimation delivers a stack of flat beams separated by dark regions. Using the diode laser stacks with 25 individual diode laser bars at 50 W CW each, 1.25 kW of optical output is delivered from an area roughly 10×40 mm. In this case, the heat flux at the mounting area can reach 313 W/cm<sup>2</sup>. At 50 W CW per bar, the electro-optical efficiency reaches about 50 percent. This makes the diode laser the most efficient artificial light source in general. Along with the development of high power diode lasers, high temperature diode lasers have been obtaining attention in recent years. Coherent Semiconductor Group has developed a proprietary device architecture that allows aluminum-free laser diodes to run at temperatures upwards of 60°C while maintaining high electro-optical efficiency. Tested at 50 W in quasi-continuous wave (QCW) mode at 808 nm to temperatures as high as 75°C, the Aluminum-free Active Area diodes offer high performance and reliability [10].

Threshold current is a very important parameter in semiconductor diode lasers. Below threshold, light output power is very inefficient, and most energy in the driving current is lost as heat. The relation between the light output power and current is schematically shown in Figure 1.1. Light emission is much more efficient above the threshold, so more of the input electrical energy is converted to light. The higher the laser threshold, the more electrical power is lost as heat. For most diode lasers the threshold current increases exponentially with increased temperature. Therefore, for a fixed driving current, increasing the temperature of the diode laser will decrease its output power. Another parameter affected by changes in the temperature is differential quantum efficiency,  $\eta_D$ , which is defined as the ratio of photon output rate to electron input rate. The differential quantum efficiency can be related with the slope of the light-current (L-I) curve in Figure 1.1:  $\eta_D = cIP/(I - I_{th})$  where  $c$  is a constant and  $\lambda$  is the lasing wavelength depending on the material's band gap. The differential quantum efficiency decreases as the temperature increases, typically at a rate of 0.5-1.0% per degree Celsius for most diode lasers. For commonly used diode materials, increasing the temperature of the diode laser results in a longer lasing wavelength. It should be pointed out that changes in the temperature can make a diode laser “hop” from one dominant mode to an adjacent one. This causes undesirable instability in laser power and output wavelength.

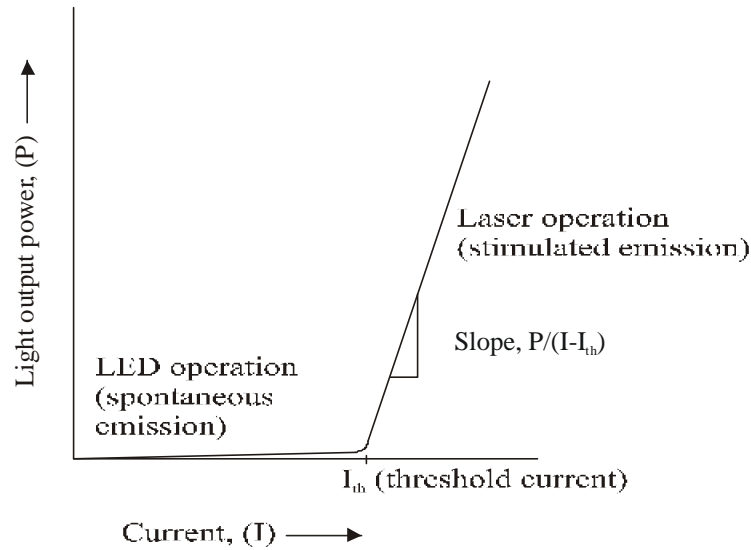


Figure 1.1 Light output of a semiconductor diode laser above and below laser threshold current.

Figure 1.2 quantitatively shows the L-I curve and electro-optical conversion efficiency of a quasi-cw 807 nm wavelength GaAs:AlGaAs bar [11]. The bar consists of 105- $\mu\text{m}$ -wide emitting regions on 120- $\mu\text{m}$  centers. The array is operated at 25°C in 200  $\mu\text{s}$  pulses at a repetition rate of 50 Hz (duty factor = 1%). At its operating power of 70 W, the conversion efficiency approaches 54%. Above the threshold current, the light output power increases almost linearly with an increase of the current and the conversion efficiency increases with the current too within the indicated current variation. It should be noted that there is the peak conversion efficiency at the optimum current for a given unit of diode laser array. In case the current injection is beyond the optimum value, the fraction of ohmic losses increases with increasing the current. The increased ohmic loss results in increased heat dissipated near the pn junction, raising the temperature of the active region and lowering its conversion efficiency. Eventually the optical output saturates and even decreases with increasing the current. Moreover, the temperature of the diode laser should not be so high as to overheat laser junctions, which leads to reduced reliability, wavelength drift and accelerated failure of the device. The normal operating temperature range for diode lasers is 15°C to 45°C [12]. Some high temperature diode lasers operate at temperatures up to 75°C [10]. From the point of view of enhancing their



lifetime, diode lasers should be operated significantly below their catastrophic damage level.

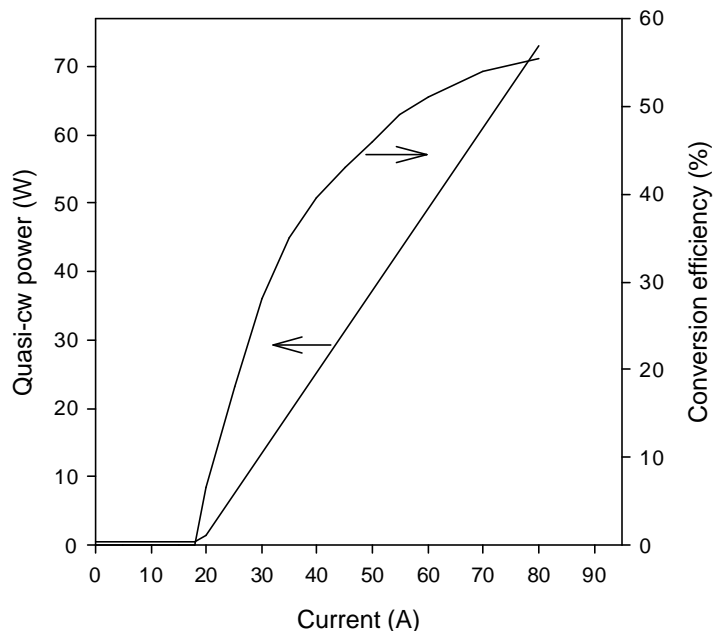


Figure 1.2 L-I curve of a quasi-cw laser array bar emitting near 807 nm wavelength, showing a conversion efficiency above 50% [11].

Almost all semiconductor lasers operate to higher peak output powers under pulsed operation than under CW operation, regardless of beam quality specification. This fact also reveals the importance of proper heat-sinking and temperature control in order to maximize laser performance at high drive levels. A typical size of a single diode laser is of the order of 100  $\mu\text{m}$  to 1000  $\mu\text{m}$  long by 100  $\mu\text{m}$  to 400  $\mu\text{m}$  wide by 50  $\mu\text{m}$  to 200  $\mu\text{m}$  thick. For a typical high power emitter, the light-emitting area is approximately 1  $\mu\text{m}$  thick and 50 to 150  $\mu\text{m}$  wide. These typical diodes have been made and tested at Fraunhofer Institute for Laser Technology in Aachen, Germany, and Coherent Inc. in Santa Clara, CA. A typical diode laser bar manufactured at Industrial Microphotonics Company in St. Charles, MO, has the dimension of 10mm long by 0.7 mm to 1.0 mm wide by 50  $\mu\text{m}$  to 200  $\mu\text{m}$  thick. A packaged diode laser stack consists of tens of the diode laser bars. The quest for ever denser package and higher output power stemming from the need of high intensity/high power beams in the defense, soldering and machining industries results in heat fluxes higher than 500  $\text{W}/\text{cm}^2$  at the

mounting surface and far higher values for the pulse laser depending on the duty cycle. Heat dissipation remains a concern for diode-laser arrays, despite their high efficiency. The cooling requirement imposes a limit on power levels available from diode lasers.

Another type of semiconductor diode laser is the vertical cavity laser, with mirrors above and below the active layer [13]. The beam emerges from the surface of the wafer. Each laser occupies only a very small area on the substrate, for example, with a diameter of 18  $\mu\text{m}$  [13]. Over a million such lasers have been packed on a single chip, with a density greater than two-million-lasers/ $\text{cm}^2$ . Room temperature CW operation of the vertical cavity laser has been achieved. The minute size of the lasers means that they may have low threshold currents which result in higher power conversion efficiency (wall plug efficiency). By introducing oxide confinement techniques, the power conversion efficiency of greater than 50% can be obtained due to the effective current confinement and the reduction of optical losses. However, due to highly dense packaging of the vertical cavity lasers, the heat flux at the chip is also high.

## **1.2 Thermal Management of High Power Diode Laser Array**

For the densely packaged diode laser bars operating at sufficiently high laser current, the heat flux at the mounting area can be higher than 500  $\text{W}/\text{cm}^2$ . Removing the heat from the diode laser array employed in the space environment requires high heat flux cooling technology and effective thermal management. The choice of cooling methods could involve liquid jet impingement cooling [14], modular micro-channel heat sink [15], and evaporative spray cooling [16]. Current packaging schemes focus on the accurate bar placement, overall thermal resistance, simplicity, ruggedness and packaging cost. A preferred packaging scheme of diode laser bars with a heat sink is shown in Figure 1.3 and Figure 1.4. The diode laser chip along with a bar bond plate is mounted between two heat spreaders. The packaged diode laser stack is bonded onto the heat sink plate. Laser beams emit perpendicularly from the heat sink plate. Coupling with the heat spreader, the heat sink plate is used to extend the heat transfer surface area and exposed to the sprayed coolant droplets. The gap between the end of the diode laser bars and the surface of the heat sink is very small compared to the diode laser array width (as shown in Figure 1.4). There is an insulating wire bond plate between the laser chip and heat sink plate to separate two opposite electrical terminals. The wire bond is related with the n-contact of the laser chip and the bar bond plate is related with the p-contact.

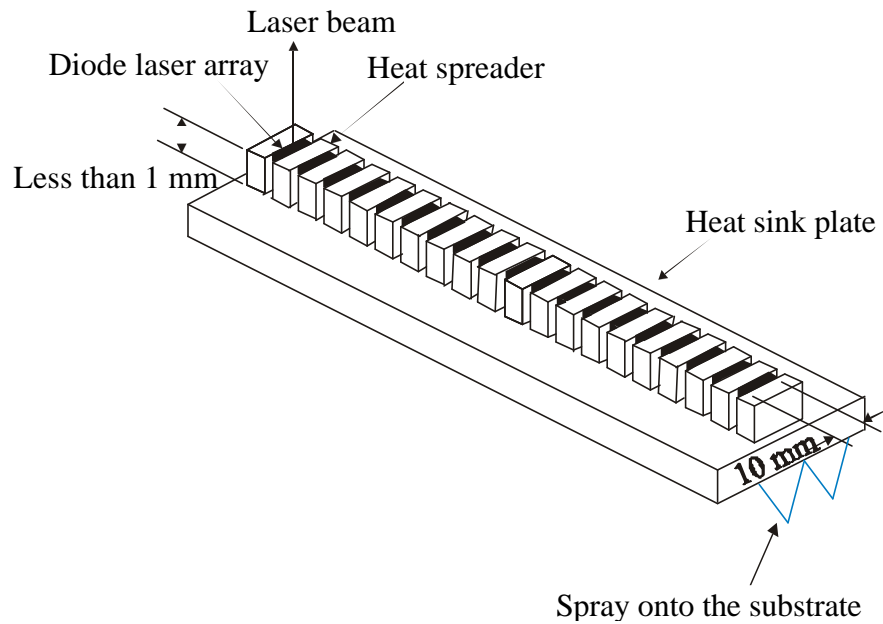


Figure 1.3 Assembly of diode laser bars in connection with heat sink.

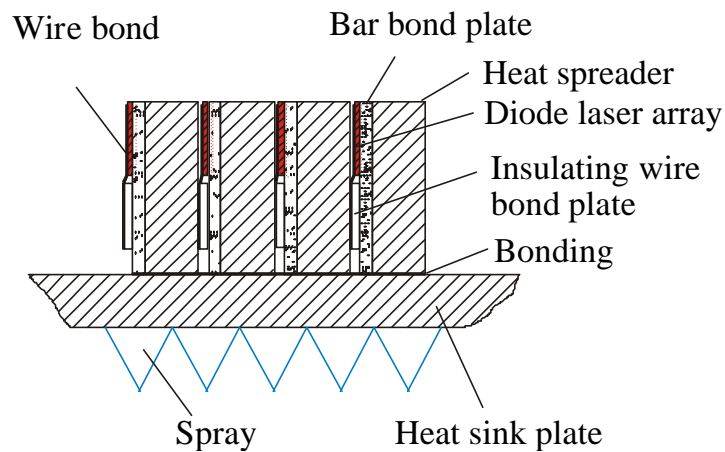


Figure 1.4 Stacking the diode laser bars.

To reduce the thermal resistance between the diode laser emitter and the cooling surface of the heat sink plate, two approaches are considered. First, we can select materials of the bar bond plate,

heat spreader and the bonding materials that have high values of thermal conductivity. An alternative is to spread the heat to a larger interface area with the heat sink through a shorter distance, either by thinning the diode laser chips or by using a heat spreader to artificially enlarge the cooling surface. The heat spreader between the semiconductor chip and the heat sink is made of a material with high thermal conductivity like diamond, carbon-carbon and copper. The heat spreader height (perpendicular to the heat sink plate) is around 1.0 mm. Given a diode laser chip, the smaller the heat spreader height, the more effective is the heat transfer from the diode laser to the mounting surface of the heat sink plate. The heat sink plate can be modified or replaced with effective phase change heat spreader, if necessary.

Another approach to enhancing the thermal limit is to modify the diode laser chip in a way that makes the laser less sensitive to increased operation temperatures. In fact, the temperature stability of the diode laser has been improved with the overall chip quality in recent years. Currently, some research institutions are developing high temperature laser materials using special epitaxial layer structures and material combinations. It is also possible to raise the thermal limit by developing desired quantum structures in the junction region.

The present heat sink of the diode laser stack is implemented using spray cooling. In spray cooling, a pressurized slightly subcooled liquid (e.g., with a subcooling smaller than 5°C) is forced through a nozzle and atomized. The resultant droplets impinge onto the heated surface. Under optimum operating conditions, approximately 20% to 30% of the liquid is vaporized upon impinging. This is a much greater percentage than for subcooled boiling so that the required flow rate is lower. The heat transfer mechanism of spray cooling is associated with phenomena such as nucleate boiling due to surface nucleation and secondary nucleation, convection heat transfer, and direct evaporation from the surface of a thin liquid film. The heat transfer coefficient of the spray cooling is high because the nucleate boiling and thin liquid film evaporation dominate the heat transfer. One of the purposes of cooling in the form of the spray is to prevent the dryout of the heated surface which results from film boiling. CHF of the spray cooling is caused by the inability of the liquid to reach the surface due to the entrainment of the countercurrent vapor flow in local regions and the splashing droplets [7]. Given a sufficiently high impingement velocity, the droplets can, up to a point, penetrate the developing vapor film on the heated surface and delay surface dryout, thereby increasing the critical heat flux.

### 1.3 Scope of the Present Research

This research deals with the multi-nozzle spray cooling of high power semiconductor diode lasers in a closed loop. The spray cooling device is capable of removing heat fluxes up to  $500 \text{ W/cm}^2$  from a hot surface and upgradable to be used in the space environment. The closed loop is designed to handle the two phase flow circulation involving evaporation and condensation. Heat transfer characteristics and CHF of the spray cooling on the hot surface are experimentally investigated. The effect of the noncondensable gas on the heat transfer and CHF is discussed. The major objectives of the present effort are presented as follows.

- ◆ Design a multi-nozzle plate with miniature nozzles to generate a spray array for the cooling of high power diode lasers.
- ◆ Develop a compact spray chamber and closed loop spray cooling system.
- ◆ Demonstrate multi-nozzle spray pattern through visualization experiment.
- ◆ Experimentally investigate heat transfer characteristics and CHF of the multi-nozzle spray cooling system using different working fluids.
- ◆ Develop a semiempirical correlation of CHF using the present experimental data.
- ◆ Reveal the effect of noncondensable gas on the thermal performance of the spray cooling system with FC-72 as the working fluid.

## 2 MULTI-NOZZLE ASSEMBLY DEVELOPMENT

### 2.1 Multi-nozzle Assembly Design

A hot surface area of  $1 \times 2 \text{ cm}^2$  is designed for the spray cooling test. To generate a spray array impinging on the cooling surface, eight miniature nozzles are made in a multi-nozzle plate as shown in Figure 2.1. Each nozzle has a swirler insert of 3.18 mm in diameter and 1.0 mm thick as shown in Figure 2.2. There are three swirl ports and one center port with a diameter of 0.2 mm in the swirl insert. The distance between the center port and a swirler port is 0.46 mm on the inner surface of the swirler insert. The tilt angle of the swirl port (with reference to the axis of the swirler insert) is  $45^\circ$ . The nozzle array is assembled by pressing the swirler inserts into the counter sinks of the multi-nozzle plate. Figure 2.3 shows the multi-nozzle plate. The nozzle discharge orifice diameter is 0.25 mm. The inner cone angle of the swirl chamber is  $60^\circ$ . The distance between two nozzles is 5.0 mm.

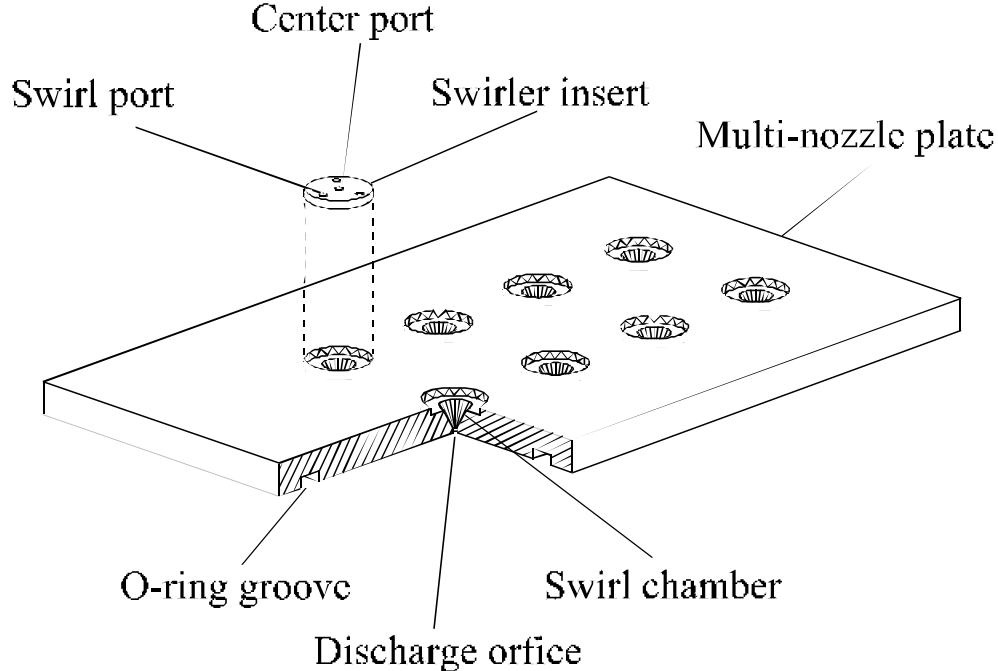


Figure 2.1 Multi-nozzle assembly.

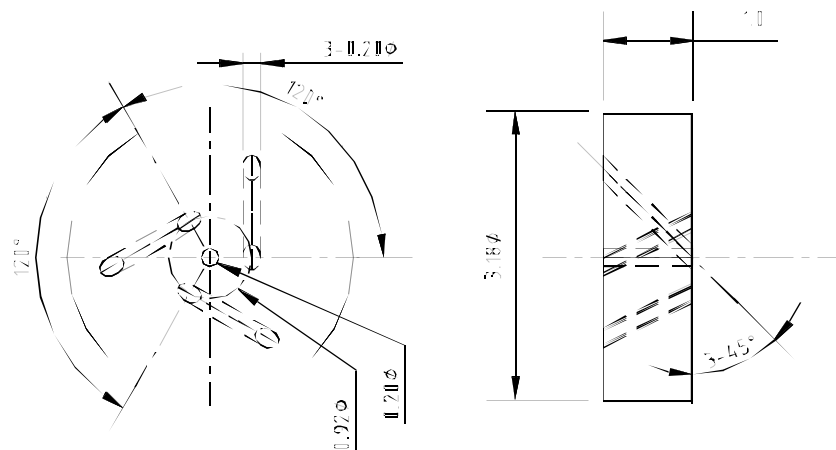


Figure 2.2 Swirler insert (dimensions in mm).

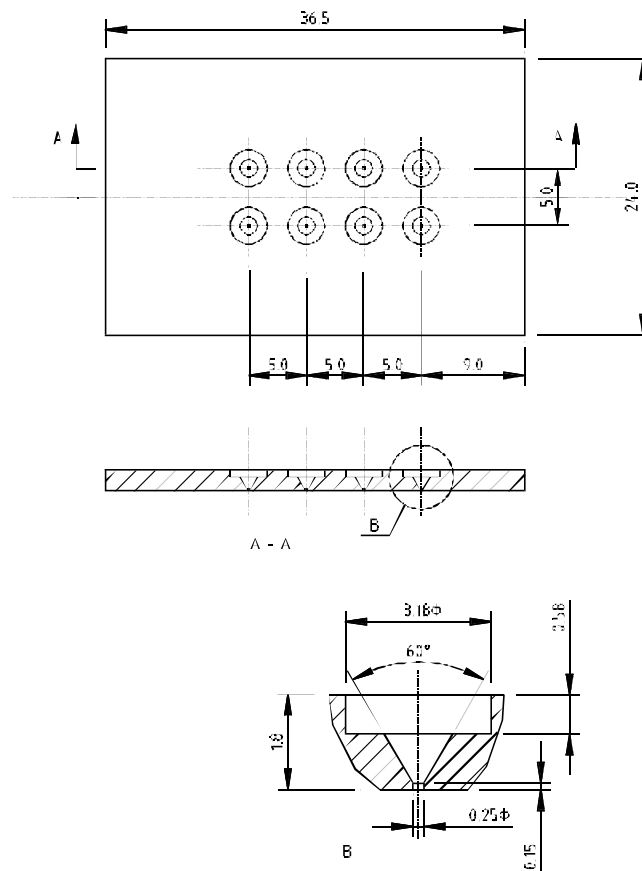


Figure 2.3 Multi-nozzle plate (dimensions in mm).

During operation, the center jet flows along the axis of the nozzle and the swirled jets from the swirl ports flow next to the wall of the swirl chamber. These jets interact in the swirl chamber and at the discharge orifice generating a swirl flow pattern. The swirling liquid jet coming out from the discharge orifice results in a wide spray cone angle (greater than  $30^\circ$ ) and intensifies liquid breakup into fine droplets at a short distance of the spray.

Nozzle Geometric Parameter Selection: The nozzle geometric parameters are selected through a series of spray tests using single nozzle. During the tests, water and FC-72 are used as the working fluids and the nozzle geometric parameters are varied as shown in Table 2.1.

Table 2.1 Nozzle geometric parameters.

Geometric parameters	Tested values	Optimum values
Center and swirl ports diameter (mm)	0.17, 0.2, 0.34	0.2
Swirl port tilt angle ( $^\circ$ )	30, 45, 50	45
Swirl chamber cone angle ( $^\circ$ )	60, 90, 108	60
Discharge orifice diameter (mm)	0.2, 0.25, 0.3, 0.35, 0.4	0.25 or 0.3

The spray is generated in the open environment at the nozzle pressure drops from 1.72 bar to 3.45 bar. The criterion of selecting the optimum nozzle geometric parameters is to generate a full cone spray with the largest spray cone angle at a given pressure drop greater than 1.72 bar. Based on this criterion, the optimum geometric parameters are obtained as shown in Table 2.1. The center port diameter and swirl port tilt angle are shown in Figure 2.2. The swirl chamber cone angle and discharge orifice diameter are shown in Figure 2.3. Figure 2.4 shows a water spray pattern of a nozzle with a 0.3 mm orifice diameter and the other optimum geometric parameters (shown in Table 2.1) at a 2.76 bar pressure drop. The nozzle is capable of generating the full cone spray pattern with very fine droplets. To limit the flow rate of the multi-nozzle array, the smaller discharge orifice diameter of 0.25 mm has been selected.



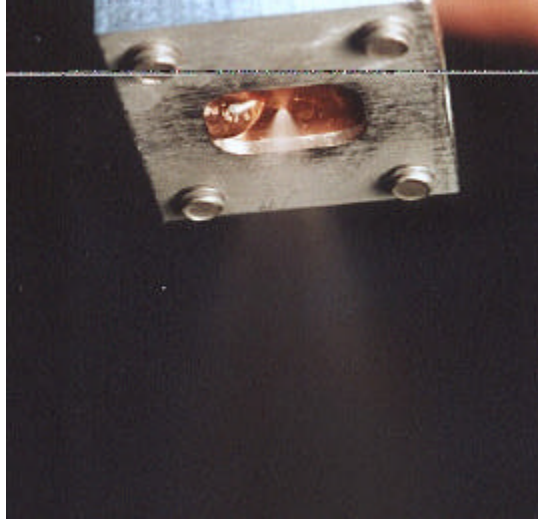


Figure 2.4 Water spray pattern of a desired nozzle at a 2.76 bar pressure drop.

## 2.2 Multi-nozzle Spray Characteristics in the Atmosphere

Spray patterns of the eight-nozzle array in the atmospheric environment are observed using FC-87, FC-72, FC-75 and water at various liquid supply pressures. It is exhibited that the nozzles are capable of generating the full cone spray patterns with spray cone angles larger than  $35^\circ$  at the nozzle pressure drops greater than 1.72 bar. In the case of the FC-72 spray at the nozzle pressure drop of 2.76 bar, an average spray cone angle of  $50^\circ$  is obtained as shown in Figure 2.5. Each nozzle generates a slightly different spray pattern as a result of dimensional uncertainty of fabricating the nozzles. It is anticipated that the multiple nozzles with the identical geometric parameters can be made using a state-of-the-art machining technique employed for micro-electro-mechanical systems (MEMS). At the pressure drop of 1.72 bar, the liquid jet velocities at the nozzle discharge orifice are greater than 70 m/s for all the tested fluids. It is believed that the disintegration of the swirling liquid jet into the fine spray droplets at a pressure drop greater than 1.72 bar is mainly caused by dynamic forces of the ambient medium. A tiny spherical drop is more stable because it has the least surface energy. A spectrum of drop diameter can experimentally be determined using a Phase Doppler Particle Analyzer (PDPA) [6]. The interaction between the spray and ambient medium results in a curved spray cone in

the region adjacent to the nozzle exit. It is observed that at the pressure drop of 1.72 bar, sufficiently fine droplets have developed at a spray distance of 8 mm (from the nozzle exit). The higher the pressure drop, the greater is the spray cone angle and the shorter is the spray distance necessary for developing sufficiently fine droplets.

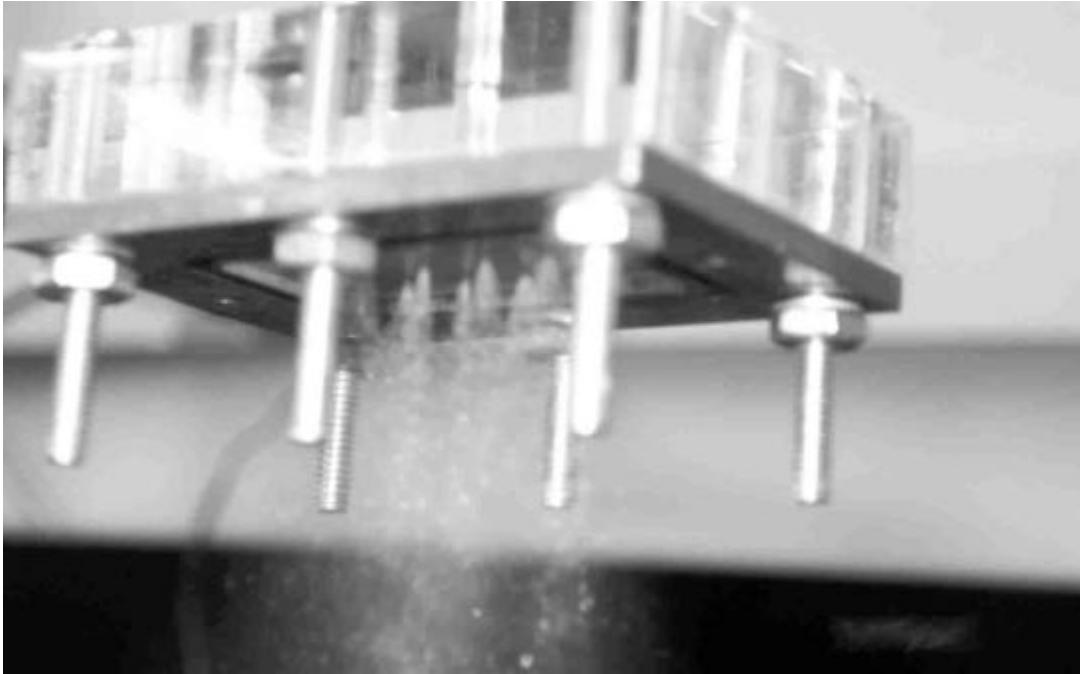


Figure 2.5 Eight-nozzle spray pattern with FC-72 as the working fluid at the pressure drop of 2.76 bar.

During the spray in the atmospheric environment, the pressure drop across the eight nozzles is measured using a pressure gauge with an uncertainty of 0.069 bar. The flow rate is measured employing a turbine flow meter whose uncertainty is 3% of reading. A measured relation between the liquid flow rate and pressure drop is shown in Figure 2.6 where  $d_i$  is the diameter of the swirl ports and the center port,  $d_0$  is the diameter of the discharge orifice and  $\vartheta$  is the swirl chamber cone angle. The curves for FC-72 and FC-75 stay closely with each other. For a given pressure drop, the flow rate for water is much higher than that for fluorocarbon fluids. The increase of the flow rate with the pressure is more significant for water than for the fluorocarbon fluids.

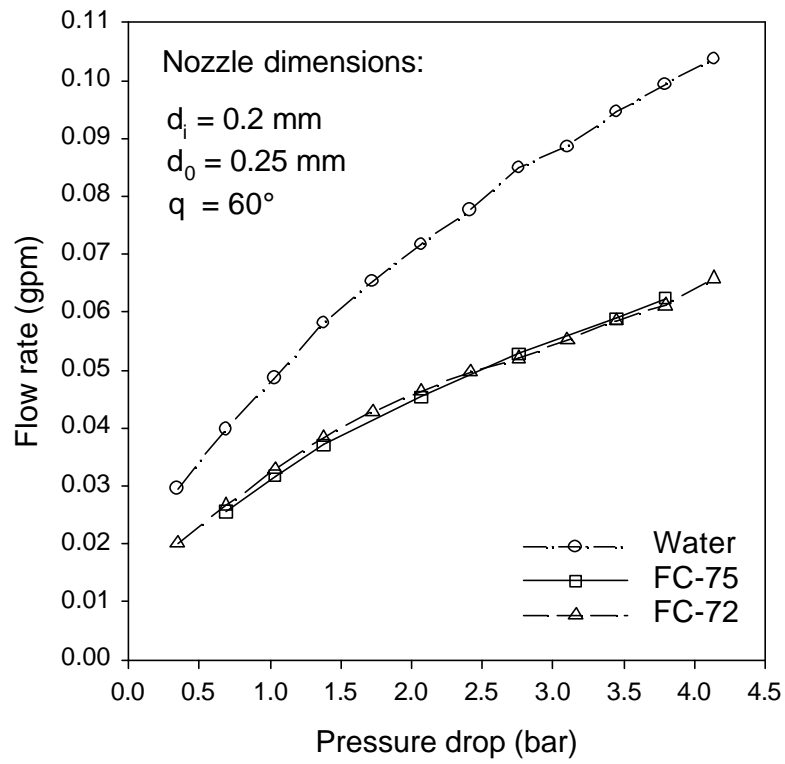


Figure 2.6 Relation between liquid flow rate and pressure drop across the eight nozzles for the spray into the atmospheric environment.

### 3 EXPERIMENTAL SETUP AND PROCEDURE

#### 3.1 Thermal Performance Test Setup

The test setup is designed for the measurement of CHF and the thermal performance of the multi-nozzle spray cooling. A photographic view of the test setup is shown in Figure 3.1. The schematic of the test setup is shown in Figure 3.2. The system consists of the multi-nozzle plate (described in Section 2), a heater assembly, a liquid chamber, a spray chamber, a helical coil condenser, flow channels (for two-phase flow and liquid flow), a magnetic gear pump, a preheater, a bypass loop, and a filter. A cold bath is used to supply cooling water to and from the condenser. The spray chamber is connected with the heater plate which is on the top of the heater block (heat focusing block).

The hot surface of the heater plate is polished with 14  $\mu\text{m}$  grit SiC paper before testing. It is noted that the same emery paper was used for surface polish in the single nozzle spray test [4]. The distance between the nozzle exit and the hot surface is 8.8 mm which is sufficiently high for breaking up the liquid jet into fine droplets. The spray chamber space dimensions are 8.8 mm (high), 28.5 mm (long) and 17.0 mm (wide). A small spray chamber is desired from the point of view of avoiding the possibility of two-phase flow oscillation as well as making the cooling device compact. Working fluids include FC-87, FC-72, methanol and water. The system of the closed loop is evacuated to a pressure below  $5 \times 10^{-6}$  Torr of before filled with the working fluid. The liquid fill amount is 190 ml which is about 38% of the internal volume of the loop. The pressure difference generated by the micro-pump maintains the circulation flow. The multiple sprays interfere with adjacent ones in the near surface region. The liquid with an elevated pressure is accumulated in the liquid chamber before ejecting through the nozzles so that each nozzle will approximately contribute the same momentum to the spray chamber. In the spray chamber, the slightly subcooled droplets impinge onto the hot surface. A large part of the droplets turn into a thin film on the hot surface and a small part of them vaporize, removing the heat through phase change. The vapor flows along with the liquid out of the spray chamber into the two-phase channel which guides the two-phase flow to the condenser where the vapor condenses. The subcooled liquid from the condenser is pumped back to the liquid chamber. The spray cooling capability is limited by CHF from the hot surface.

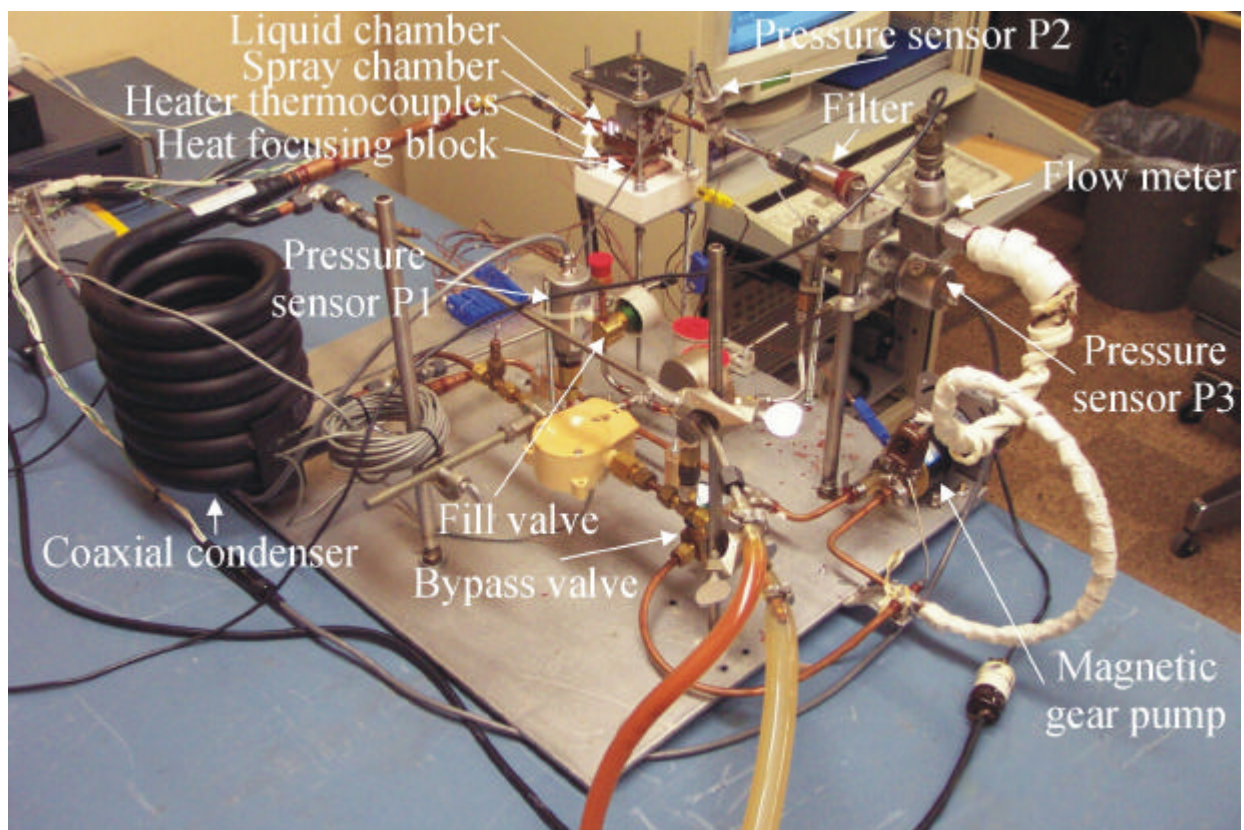


Figure 3.1 Photographic view of the test setup.

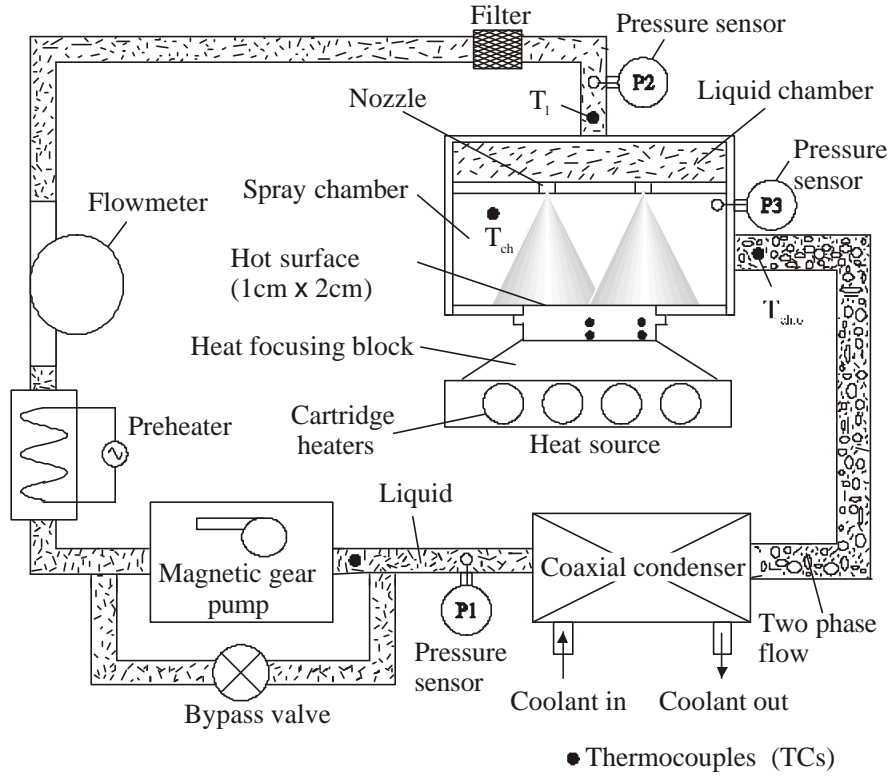


Figure 3.2 Schematic of test setup.

The liquid flow rate of the spray cooling system is measured using a turbine flow meter operating with a signal conditioner. The spray chamber pressure ( $p_3$ ), the pressure at the inlet of the liquid chamber ( $p_2$ ) and the pressure at the outlet of the condenser ( $p_1$ ) are measured using three pressure sensors. The spray chamber pressure corresponds to the fluid saturation temperature,  $T_{sat}$ , in the spray chamber. The spray pressure drop, the pressure difference between the supply pressure ( $p_2$ ) and spray chamber pressure ( $p_3$ ), is controlled by the pump and bypass valve. The rotational speed of the magnetic pump is adjustable through a DC power supply. The working fluid temperatures at the four locations in the spray cooling loop are measured using T-type probe thermocouples as shown in Figure 3.2. The supply liquid temperature (at the inlet of liquid chamber),  $T_1$ , is regulated by adjusting the flow rate and temperature of the cooling water and the input power to the preheater. It is desired

that  $T_1$  is set to be as close to  $T_{\text{sat}}$  as possible to minimize the subcooling effect. The spray chamber temperature,  $T_{\text{ch}}$ , is used for monitoring only.

The copper heater block with four cartridge heaters is used as the heat source. Each cartridge heater with 6.35 mm in diameter and 38.1 mm long can deliver power up to 250 W. The heater plate with the hot surface towards the spray chamber is embraced by an insulation plate made of silicone and glass, G7, and is tightly attached to the heater block by a compression assembly. Thermal grease is used to minimize the contact thermal resistance between the heater plate and heater block. Figure 3.3 shows the dimensions of the insulation plate which forms the bottom side of the spray chamber. Figure 3.4 shows the dimensions of the heater plate. Eight thermocouples are embedded in 0.58 mm holes drilled along two planes in the heater plate, forming four pairs of thermocouples. Four thermocouple locations in the front of the heater plate are shown in Figure 3.2 and Figure 3.4. The distance between two thermocouple location planes,  $t_2$ , is 2.54 mm as shown in Figure 3.4. The distance between the hot surface and the upper plane of the thermocouple locations,  $t_1$ , is 2.16 mm. The thermocouple bead diameter is 0.3 mm. The heater assembly is well insulated with fiberfrax. The hot surface heat flux or the heat rate per unit hot surface area is calculated by

$$q'' = \frac{c_w k_h}{t_2} (T_{2,m} - T_{1,m}), \quad (1)$$

where  $T_{1,m}$  and  $T_{2,m}$  are the arithmetic means of the temperatures indicated by the four thermocouples at the upper plane and those at the lower plane, and the constant  $c_w$  is obtained through calibration (described in Section 3.3). The average temperature on the hot surface,  $T_w$ , is calculated by

$$T_w = T_{1,m} - \frac{q'' t_1}{k_h}. \quad (2)$$

AC power is applied to the cartridge heaters. The AC voltage is adjustable through a variac. The input power is monitored by a power analyzer (MAGTROL). For the safe operation, one of the thermocouples measuring the temperatures in the heater plate is connected to a high temperature cut out unit. If the temperature is higher than a set limit, the power supply will automatically cut out.

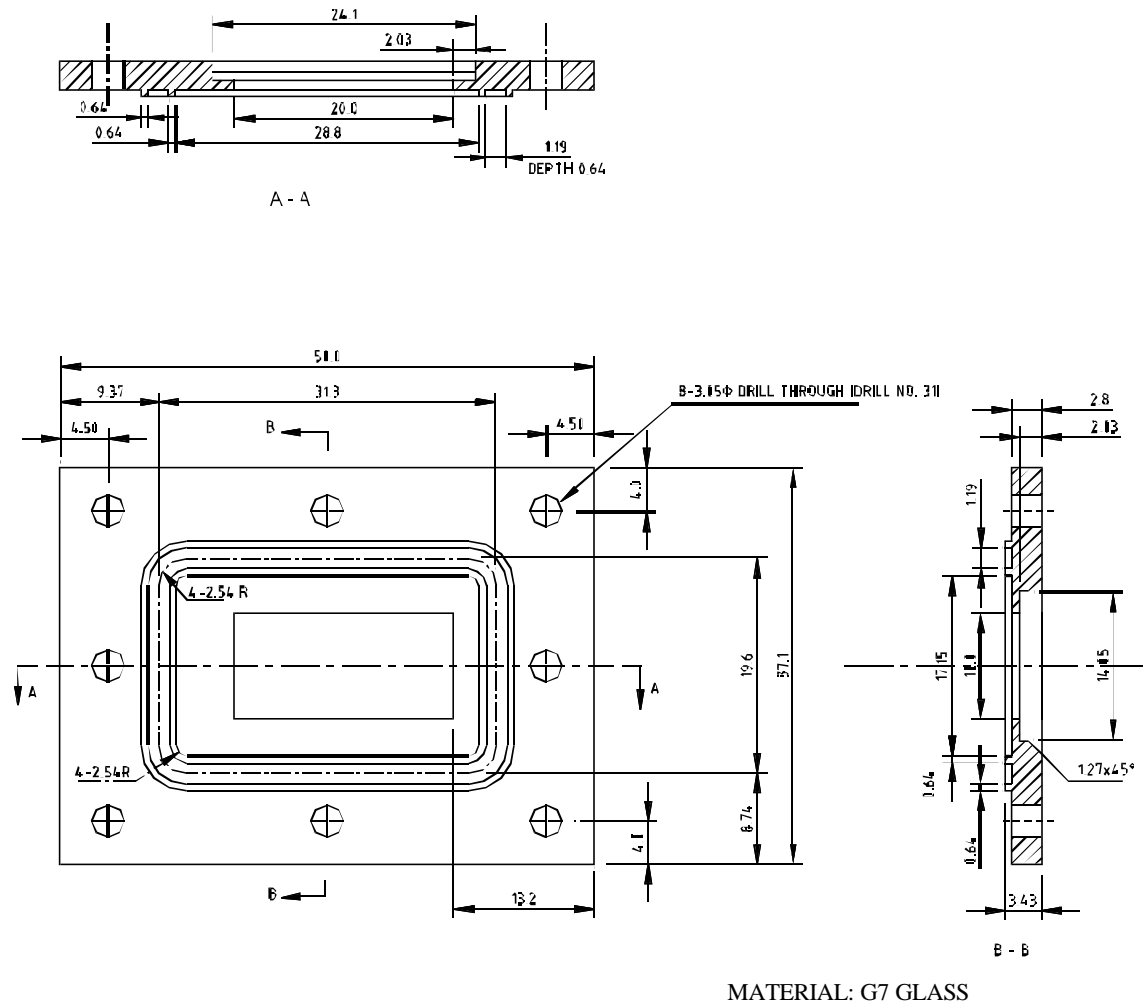


Figure 3.3 Insulation plate (dimensions in mm).



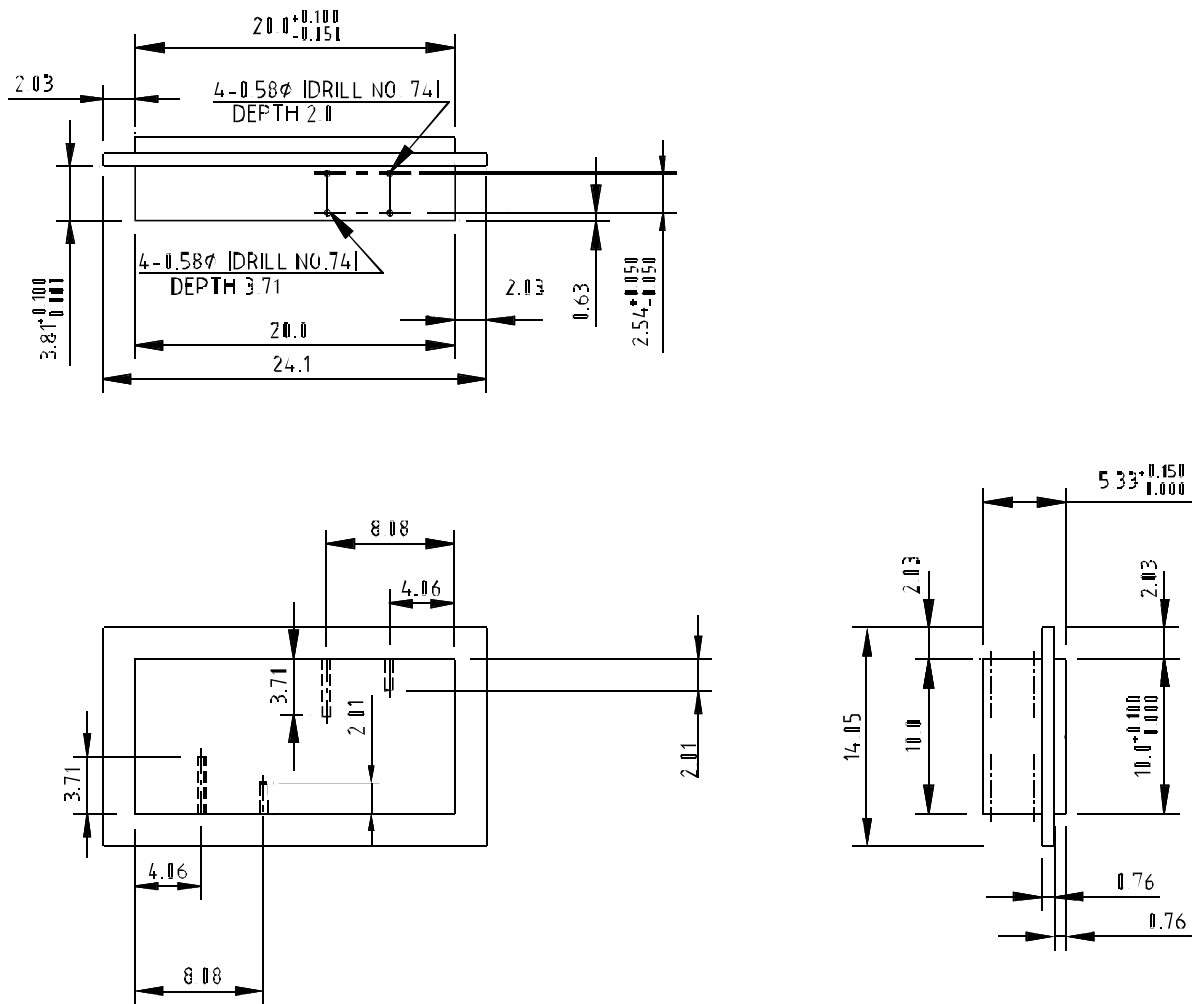


Figure 3.4 Heater plate with thermocouple holes (dimensions in mm).

All signals of the measured parameters are transferred to PC for recording through an HPIB interface card. During the test, the input power is varied from 20 W to 1020 W or up to the amount relating with CHF. The spray pressure drop is adjusted at the levels of 0.69 bar, 1.03 bar, 1.72 bar, 2.41 bar and 3.1 bar. The spray chamber pressure is varied according to the working fluid being used. All data are acquired 50 times in an interval of 1 minute and the average values are recorded after a steady state is reached.

### **3.2 Visualization Setup**

To observe the spray pattern in the spray chamber, the frame of the spray chamber is replaced with a transparent material (acrylic material) with the same dimensions as the metallic frame used for the performance test. A photographic view of the visualization setup is shown in Figure 3.5. FC-72 is used as the working fluid. During visual observation, operating conditions such as the pressure drop across the nozzles, input power and spray chamber temperature are varied. In this photograph, the devices around the spray chamber are magnified. The observed flow pattern is discussed in Section 4.1.

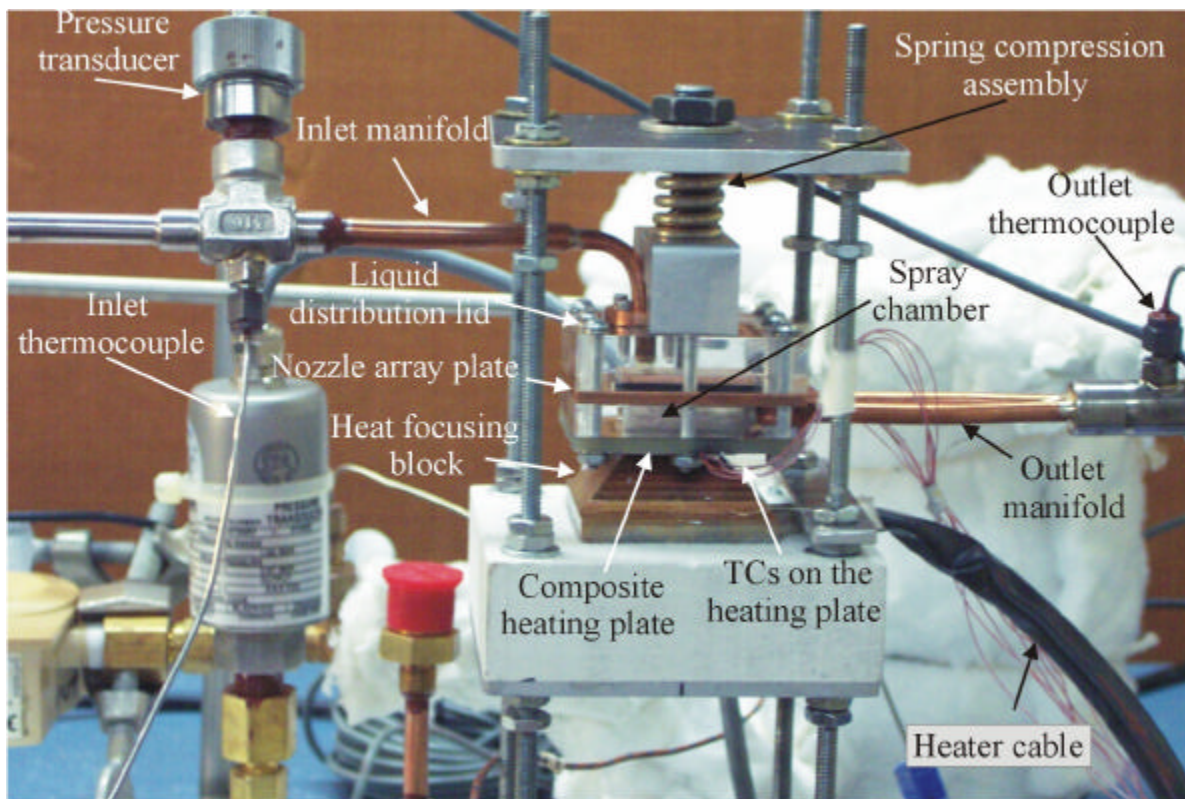


Figure 3.5 Photographic view of the visualization setup.

### 3.3 Measurement Uncertainty

A data acquisition system is used to record all temperature measurements. This device has a resolution of  $0.02^{\circ}\text{C}$ . The data acquisition unit and T-type thermocouples are compared to a precision digital resistance temperature device with  $0.03^{\circ}\text{C}$  rated accuracy. The system accuracy is found to be within  $0.2^{\circ}\text{C}$  over the range of interest. In the steady state, the thermocouples fluctuate within  $0.2^{\circ}\text{C}$ .

The uncertainty of the electrical power through the power analyzer is 0.5% of reading. The accuracy of the distance between two thermocouples in each pair in the heater plate is 0.1 mm and the accuracy of the distance between the hot surface and the upper level of the thermocouple locations in the heater plate is 0.15 mm. The uncertainty of the hot surface area of the heater plate is  $0.05\text{ cm}^2$ . To reach a lower uncertainty of the heat flux measurement, the effective distance between the upper level and lower level of the thermocouple locations is calibrated by measuring heat losses of the heater block and plate. To do this, the heater block and plate are covered with an insulation material and a small electric power load is applied to the cartridge heater. The applied electric power load is adjusted until a specific temperature of the heater block is reached. During the measurement, the heater block temperature is varied. The heat loss is 15 W at the heater block temperature of  $250^{\circ}\text{C}$ . The actual heat rate through the hot surface is estimated by subtracting the heat losses from the input power. The actual heat rate and the measured temperatures in the heater plate for the same input power are used to determine the effective distance of the thermocouple locations. The uncertainty of the heat flux is 4.8% at  $q''=50\text{ W/cm}^2$  which is the smallest CHF data obtained in the present experiment. The uncertainty of  $T_w$  is estimated within  $0.33^{\circ}\text{C}$ .

The accuracies of the pressure sensors at the inlet of liquid chamber, at the outlet of condenser and in the spray chamber are  $6.0\times 10^{-3}\text{ bar}$ ,  $2.6\times 10^{-3}\text{ bar}$  and  $8.6\times 10^{-3}\text{ bar}$ . The saturation temperature,  $T_{\text{sat}}$ , is calculated as function of the spray chamber pressure. The uncertainty of  $T_{\text{sat}}$  is estimated within  $0.3^{\circ}\text{C}$ . The turbine flow meter is calibrated for FC-72, and water. The uncertainty of the flow rate is 3% of reading. The uncertainty of  $Q''$  is estimated to be 3.9%.

## 4 RESULTS AND DISCUSSION

### 4.1 Spray Cooling Pattern in Confined Chamber

It is observed during the visualization experiment that nucleate boiling heat transfer occurs in all tested cases. The spray cones are surrounded by the agitated two-phase fluid. A schematic of a typical spray cooling pattern in the spray chamber is shown in Figure 4.1. The droplets impinge onto the hot surface and splash to the circumference of the spray. The splashing liquid is restricted by the wall and is forced to rebound to the space surrounding the sprays. It is conceivable that the interaction between the spray cone and surrounding fluid is stronger in the case of multi-nozzle spray cooling than in the case of single nozzle spray cooling. A longer spray distance may bring about a stronger interaction of the spray with the surrounding fluid and therefore may cause more momentum losses along the spray distance.

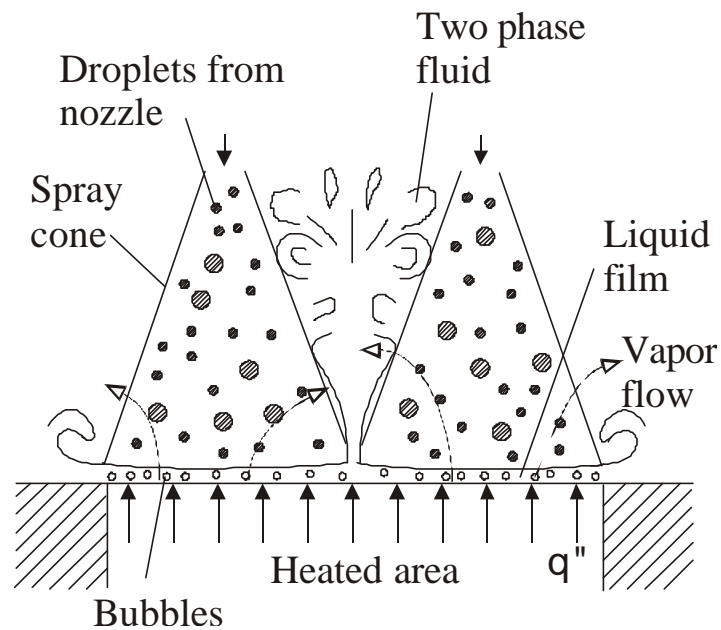


Figure 4.1 Spray cooling pattern.

## 4.2 Heat Transfer Characteristics

Experimental data expressing heat transfer characteristics,  $q''$  vs.  $T_w - T_{sat}$ , for FC-87, FC-72, water and methanol are presented in Figure 4.2 through Figure 4.14. The values of the volumetric flux,  $Q''$  ( $m^3/m^2s$ ), and the nozzle pressure drop,  $\Delta p = p_2 - p_3$ , refer to the conditions pertinent to the curves. The volumetric flux is defined as the total liquid volumetric flow rate divided by the hot surface area. Also presented in these figures are the different saturation temperatures,  $T_{sat}$ , in the spray chamber and the subcooling  $T_{sat} - T_l$ , where  $T_l$  is the liquid temperature.

Figures 4.2, 4.3, 4.4 and 4.5 are the results for FC-87. Figures 4.6, 4.7 and 4.8 are the cases for FC-72. Figures 4.2, Figure 4.3 and Figure 4.4 show the effect of volumetric flux on heat transfer characteristics for FC-87 at  $T_{sat}=42^\circ C$ ,  $T_{sat}=32^\circ C$  and  $T_{sat}=22^\circ C$ . Figure 4.6 and Figure 4.7 present the effect of volumetric flux on heat transfer characteristics for FC-72 at  $T_{sat}=53^\circ C$  and  $T_{sat}=36^\circ C$ . The values of subcooling,  $T_{sat} - T_l$ , are very small for these cases. Generally, the surface superheat,  $T_w - T_{sat}$ , increases with an increase of the heat flux,  $q''$ . For a given surface superheat, the heat flux increases with the volumetric flux. As seen from the figures, the slope of the curves varies with the superheat. In the lower superheat region, e.g.,  $T_w - T_{sat} < 15^\circ C$ , the slope of the curves is relatively small and does not change much. In this case, the heat transfer is mainly ruled by convection along with evaporation from the surface of liquid film though slight nucleate boiling occurs. As the surface superheat exceeds a point, around  $15^\circ C$ , the slope of the curves increases and then turns to decreasing. This trend indicates that the nucleate boiling heat transfer is becoming a major part of heat transfer and then the transport process involves more convection and evaporation of the liquid film until dryout occurs. At pressure drops above 1.72 bar (corresponding to volumetric fluxes between  $0.0167 m^3/m^2s$  and  $0.0181 m^3/m^2s$ ), the increase in heat flux due to an increase of the pressure drop becomes small. This is due to the fact that a higher volumetric flux results in a thicker liquid film that decreases the evaporation from the free surface, thus partially counteracts the effect of increased convection. This also implies that the pressure drop of 1.72 bar or lower may not be optimum for the maximum heat removal.

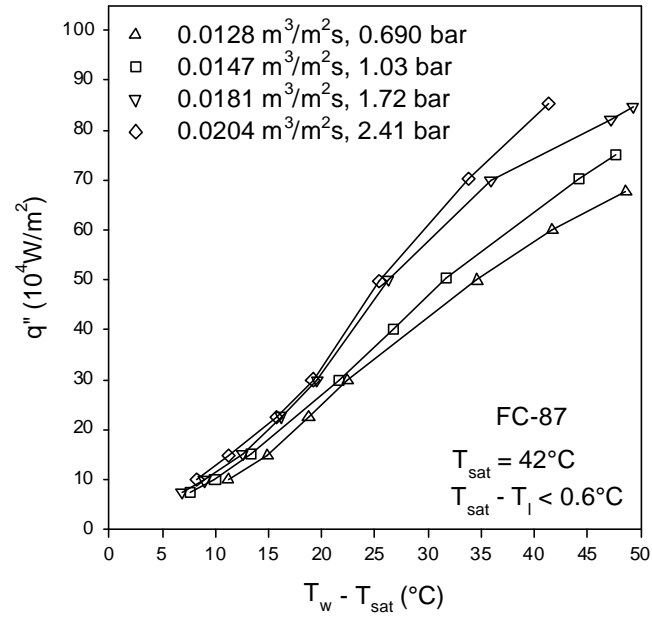


Figure 4.2 Effect of volumetric flux on heat transfer characteristics for FC-87 at  $T_{\text{sat}} = 42^\circ\text{C}$ .

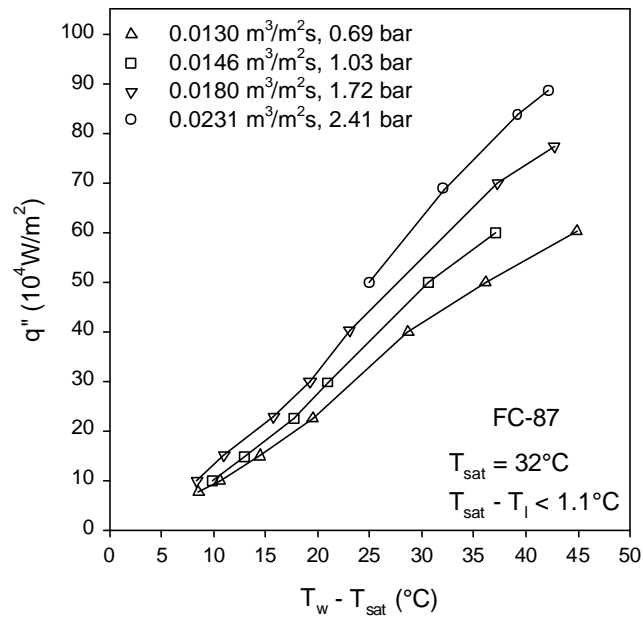


Figure 4.3 Effect of volumetric flux on heat transfer characteristics for FC-87 at  $T_{\text{sat}} = 32^\circ\text{C}$ .

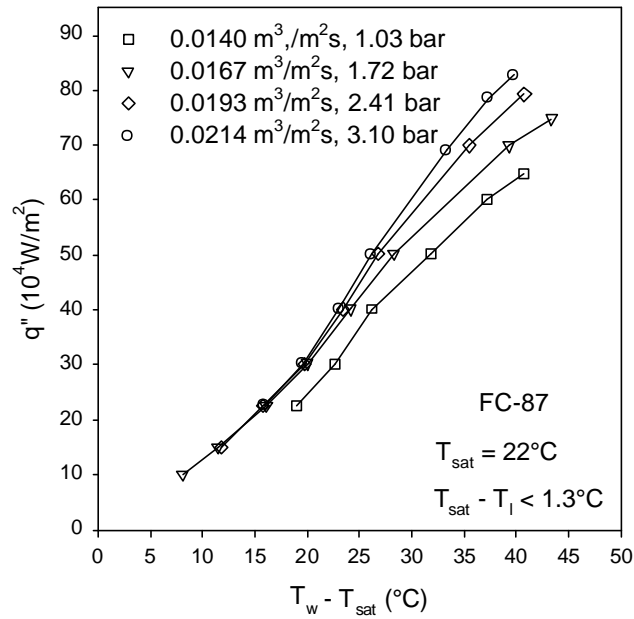


Figure 4.4 Effect of volumetric flux on heat transfer characteristics for FC-87 at  $T_{\text{sat}}=22^\circ\text{C}$ .

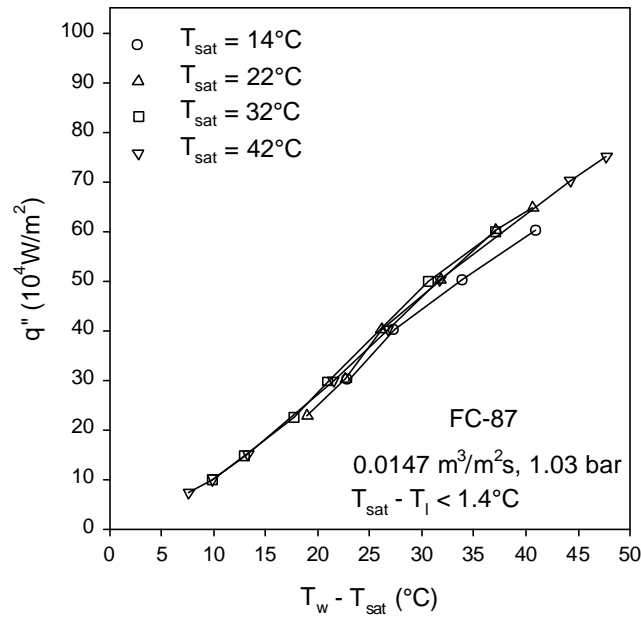


Figure 4.5 Effect of spray saturation temperature on heat transfer characteristics for FC-87 at  $\Delta p=1.03 \text{ bar}$ .



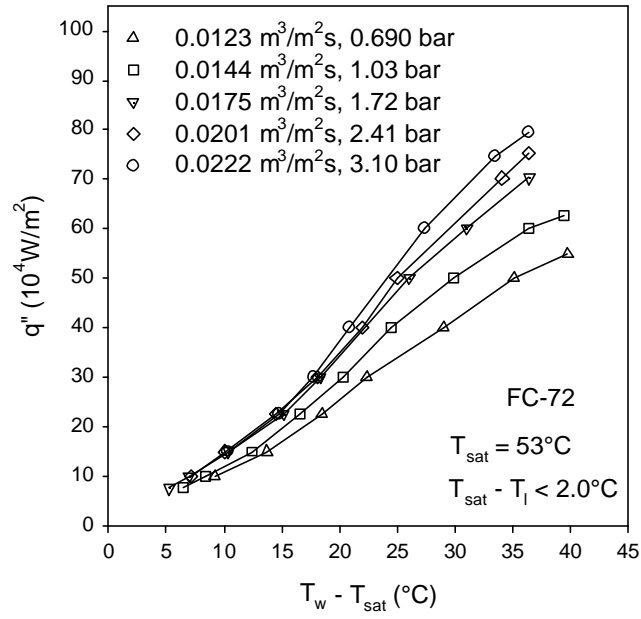


Figure 4.6 Effect of volumetric flux on heat transfer characteristics for FC-72 at  $T_{\text{sat}}=53^\circ\text{C}$ .

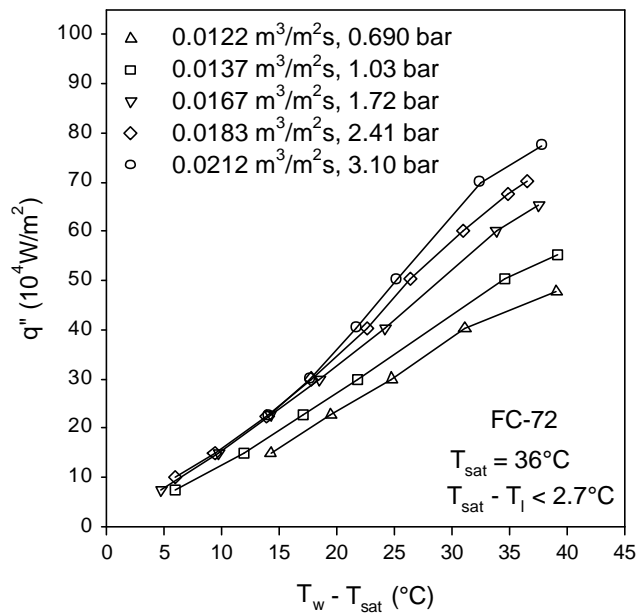


Figure 4.7 Effect of volumetric flux on heat transfer characteristics for FC-72 at  $T_{\text{sat}}=36^\circ\text{C}$ .

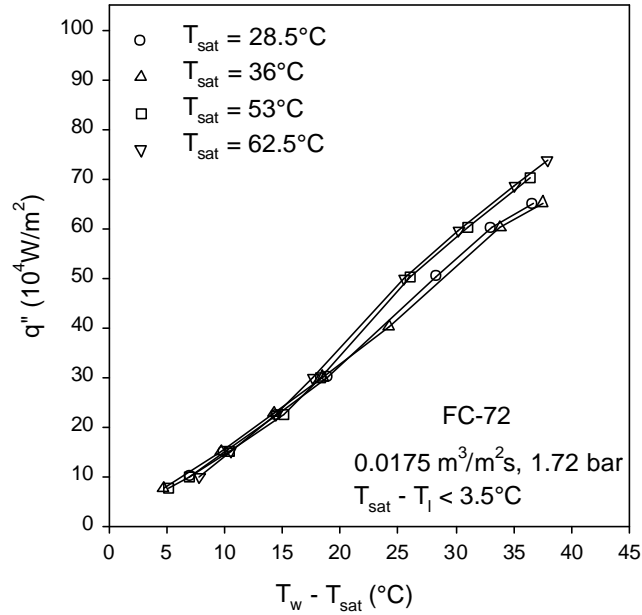


Figure 4.8 Effect of spray saturation temperature on heat transfer characteristics for FC-72 at  $\Delta p=1.72$  bar.

Figure 4.5 shows the effect of spray saturation temperature on heat transfer characteristics for FC-87 at  $\Delta p=1.03$  bar. Figure 4.8 gives the effect of spray saturation temperature on heat transfer characteristics for FC-72 at  $\Delta p=1.72$  bar. The subcooling is smaller than  $1.4^\circ\text{C}$  for FC-87 and smaller than  $3.5^\circ\text{C}$  for FC-72. It can be seen that the change in the relation of  $q''$  with  $T_w - T_{sat}$  is small with the variation of the saturation temperature at a given pressure drop. This might be attributed to the fact that the nucleation sites at the hot surface do not change much at the same volumetric flux. It is noted that the variation of the sprayed surface temperature is within  $1.5^\circ\text{C}$  for the fluorocarbon fluids (FC-87 and FC-72).

Figure 4.9 and Figure 4.10 show the effect of volumetric flux on heat transfer characteristics for methanol at  $T_{sat}=66.6^\circ\text{C}$  to  $69.0^\circ\text{C}$  and at  $T_{sat}=50.3^\circ\text{C}$  to  $53.7^\circ\text{C}$ . Figure 4.11 gives the effect of spray saturation temperature on heat transfer characteristics for methanol at  $\Delta p=1.72$  bar. The subcooling for methanol (lower than  $13.7^\circ\text{C}$ ) is still small since CHF for methanol is much higher. The relation of the heat flux with the surface superheat, as shown in Figure 4.9 and Figure 4.10, is somewhat like the cases of the fluorocarbon fluids but the achievable heat fluxes are much higher than those for FC-87

and FC-72. The variations of the slope of the curves in Figure 4.9 and Figure 4.10 reveal that the boiling heat transfer becomes important at the superheats greater than 30°C. As seen from Figure 4.11, the change in the relation of the heat flux with the surface superheat is small with the variation of  $T_{\text{sat}}$ .

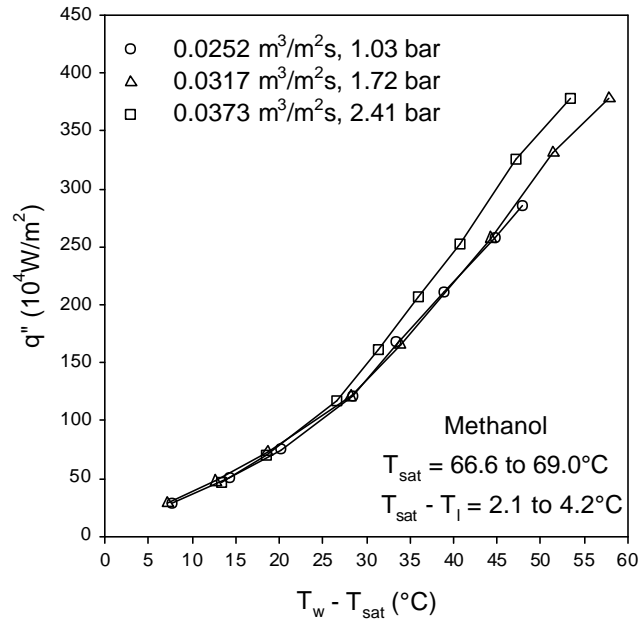


Figure 4.9 Effect of volumetric flux on heat transfer characteristics for methanol at  $T_{\text{sat}}=66.6^{\circ}\text{C}$  to  $69.0^{\circ}\text{C}$ .

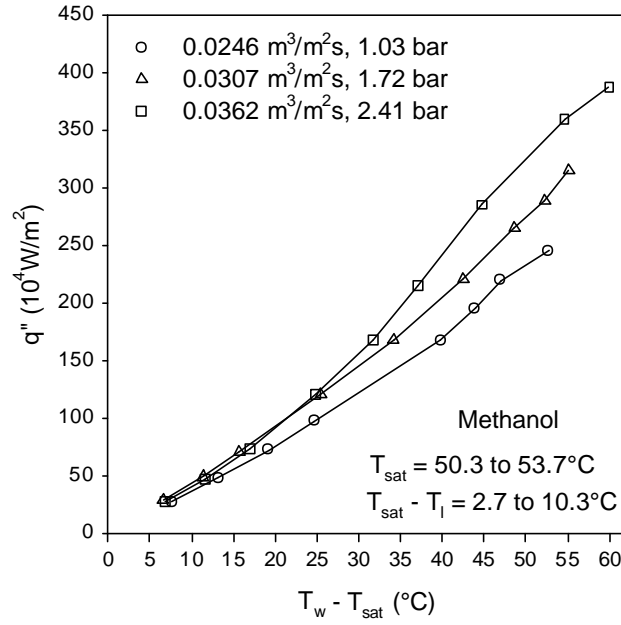


Figure 4.10 Effect of volumetric flux on heat transfer characteristics for methanol at  $T_{\text{sat}}=50.3^{\circ}\text{C}$  to  $53.7^{\circ}\text{C}$ .

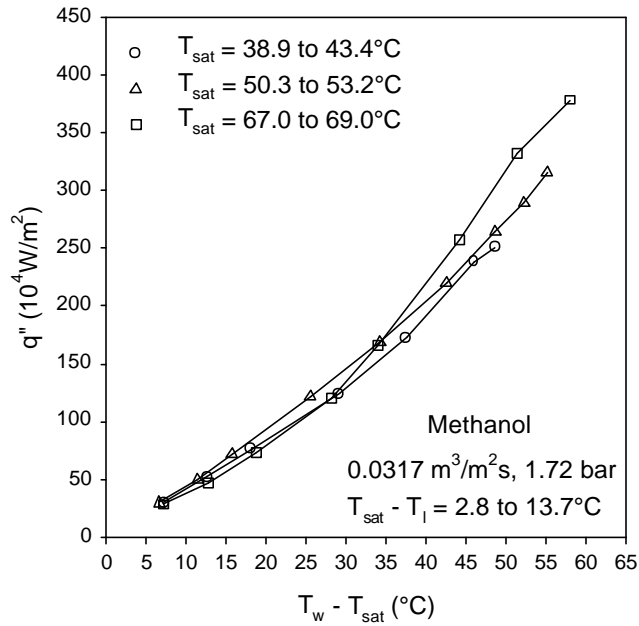


Figure 4.11 Effect of spray saturation temperature on heat transfer characteristics for methanol at  $\Delta p = 1.72 \text{ bar}$ .

Figure 4.12 and Figure 4.13 show the effect of volumetric flux on heat transfer characteristics for water at  $T_{\text{sat}}=80.5^{\circ}\text{C}$  to  $84.3^{\circ}\text{C}$  and at  $T_{\text{sat}}=67^{\circ}\text{C}$  to  $72^{\circ}\text{C}$ . Figure 4.14 gives the effect of spray saturation temperature on heat transfer characteristics for water at  $\Delta p=1.72$  bar. The subcooling for water (lower than  $17.2^{\circ}\text{C}$ ) is higher than the cases of the fluorocarbon fluids but is still considered as being small since CHF for water is much higher (greater than  $500 \text{ W/cm}^2$ ). As shown in Figure 4.12 and Figure 4.13, the surface superheat increases monotonically with an increase of the heat flux and the change in the slope of the curves is small with a variation of the superheat. The convection heat transfer along with the evaporation from the liquid film surface could be a more noticeable heat transfer mode compared to the cases of the fluorocarbon fluids. It seems similar to the cases of the fluorocarbon fluids that the pressure drop greater than 1.72 bar is required to reach high heat fluxes. Since the maximum input power is 1020 W, the data points exceeding  $500 \text{ W/cm}^2$  are not obtained for water. It may be seen from Figure 4.14 that the change in the relation of the heat flux with the superheat is still small with the variation of  $T_{\text{sat}}$  under the present operating conditions.

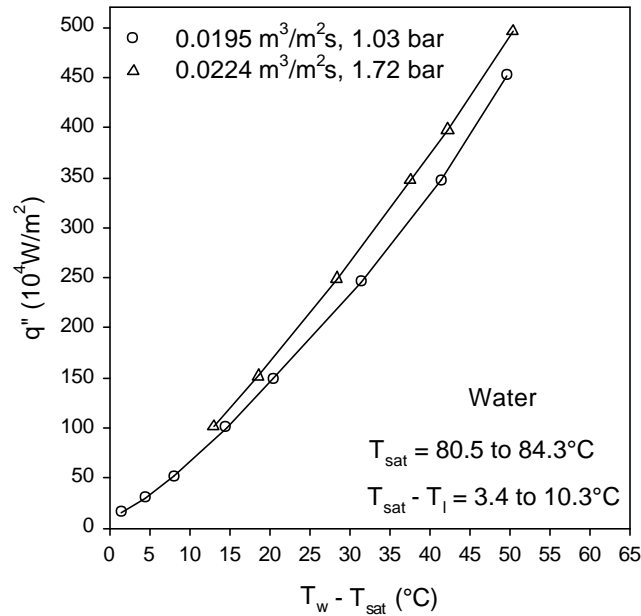


Figure 4.12 Effect of volumetric flux on heat transfer characteristics for water at  $T_{\text{sat}}=80.5^{\circ}\text{C}$  to  $84.3^{\circ}\text{C}$ .

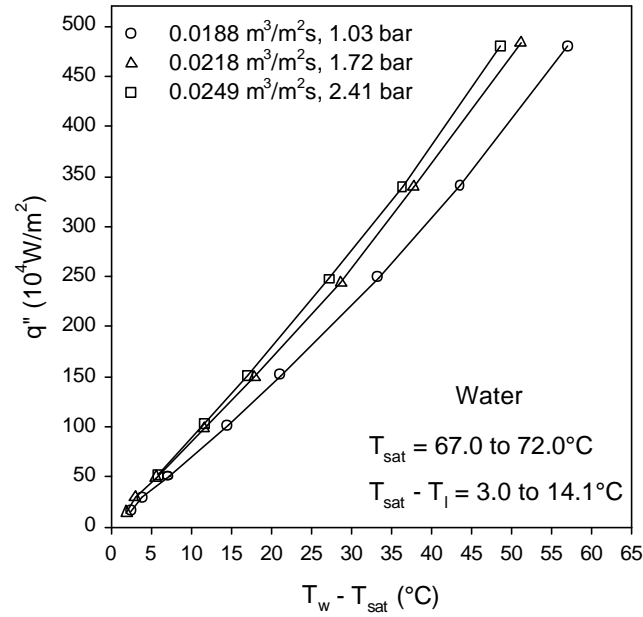


Figure 4.13 Effect of volumetric flux on heat transfer characteristics for water at  $T_{\text{sat}}=67^{\circ}\text{C}$  to  $72^{\circ}\text{C}$ .

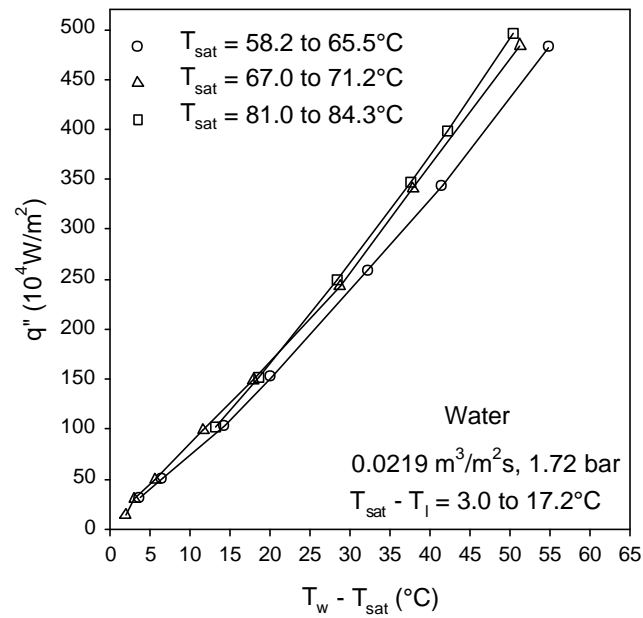


Figure 4.14 Effect of spray saturation temperature on heat transfer characteristics for water at  $\Delta p=1.72$  bar.

To obtain more spray cooling information, the effectiveness of spray cooling at CHF,  $\eta_c$ , Sauter mean diameter (SMD) [17],  $d_{32}$ , and heat transfer coefficient of the spray cooling,  $h$ , are calculated. The effectiveness of spray cooling at CHF is defined as the ratio of the heat that is actually removed at CHF to the total latent heat that could be removed by the spray and is written as

$$h_c = \frac{q''_c}{h_{fg} Q'' r_l}. \quad (3)$$

SMD is the diameter of a droplet whose volume-to-surface area ratio is the same as for the entire spray sample. The value of SMD is estimated using the following correlation [18].

$$\frac{d_{32}}{d_0} = 3.07 \left( \frac{r_v^{0.5} \Delta p d_0^{1.5}}{s^{0.5} m_l} \right)^{-0.259}. \quad (4)$$

The heat transfer coefficient of the spray cooling is defined as

$$h = \frac{q''}{T_w - T_{sat}}. \quad (5)$$

The maximum heat transfer coefficient obtained for a given saturation temperature is denoted by  $h_1$ . The results of  $\eta_c$ ,  $d_{32}$  and  $h_1$  as well as other parameters for the four tested working fluids are listed in Table 4.1. It is shown that  $\eta_c$  is much smaller and  $d_{32}$  is greater for methanol and water than for FC-87 and FC-72 at the same  $\Delta p$ . Using the same multi-nozzle array, either methanol or water has the smallest  $\eta_c$  though the values of  $\eta_c$  for water are not reached. The value of  $\eta_c$  decreases with  $\Delta p$  for FC-87, FC-72 and water but increases slightly with  $\Delta p$  for methanol. Increasing  $\Delta p$  decreases  $d_{32}$  and generates more droplets. It is exhibited from the variations of  $h_1$  with  $\Delta p$  that the spray heat transfer is enhanced with increasing the pressure drop. The highest heat transfer coefficient is obtained by using water as the working fluid. Since the subcooling of the working fluids is controlled to be as small as possible by using the preheater, the effect of the subcooling on the heat transfer coefficient is precluded from the discussion of the results.

Table 4.1 Spray cooling parameters

Working Fluid	$T_b$ (°C)	$T_{sat}$ (°C)	$\Delta p$ (bar)	$Q''$ (m <sup>3</sup> /m <sup>2</sup> s)	$d_{32}$ (μm)	$q''_c$ (CHF) (W/cm <sup>2</sup> )	$\eta_c$ (-)	$h_l$ (10 <sup>3</sup> W/m <sup>2</sup> K)
FC-87	30	42.5	1.03	0.0147	45.3	79.0	0.374	15.8
			1.72	0.0181	39.6	87.5	0.336	19.5
			2.41	0.0204	36.5	90.0	0.306	20.6
FC-72	56	54	1.03	0.0144	52.1	65.0	0.324	16.7
			1.72	0.0175	45.2	72.5	0.300	19.4
			2.41	0.0201	41.4	78.5	0.282	20.7
			3.10	0.0222	38.7	83.5	0.271	22.3
Methanol	65	53	1.03	0.0246	79.6	357.5	0.122	46.8
			1.72	0.0308	68.6	440	0.131	57.2
			2.41	0.0363	62.3	490	0.133	64.5
Water	100	70	1.03	0.0188	111	>500	>0.116*	84.2
			1.72	0.0218	96.9	>500	>0.101*	94.6
			2.41	0.0249	88.8	>500	>0.088*	97.8

\* at 500 W/cm<sup>2</sup>

### 4.3 Critical Heat Flux

Experimental data of CHF,  $q''_c$ , for FC-87, FC-72 and methanol are plotted in Figures 4.15, 4.16 and 4.17, as function of the volumetric flux,  $Q''$ . Also presented in these figures are the different saturation temperatures,  $T_{sat}$ , in the spray chamber and the supply liquid temperatures,  $T_l$ . For FC-87 and FC-72, the values of subcooling,  $T_{sat}-T_b$ , are very small (less than 3.5°C). For methanol, the subcooling is relatively higher (between 4°C and 12°C) but still considered as being small since CHF for methanol is much higher. Generally, CHF increases with an increase of the volumetric flux and saturation temperature under the present condition. In these figures, the highest CHF value is 91.5 W/cm<sup>2</sup> for FC-87, 83.5 W/cm<sup>2</sup> for FC-72 and 490 W/cm<sup>2</sup> for methanol. For the fluorocarbon fluids, all the curves at various  $T_{sat}$  levels tend to merge with each other.



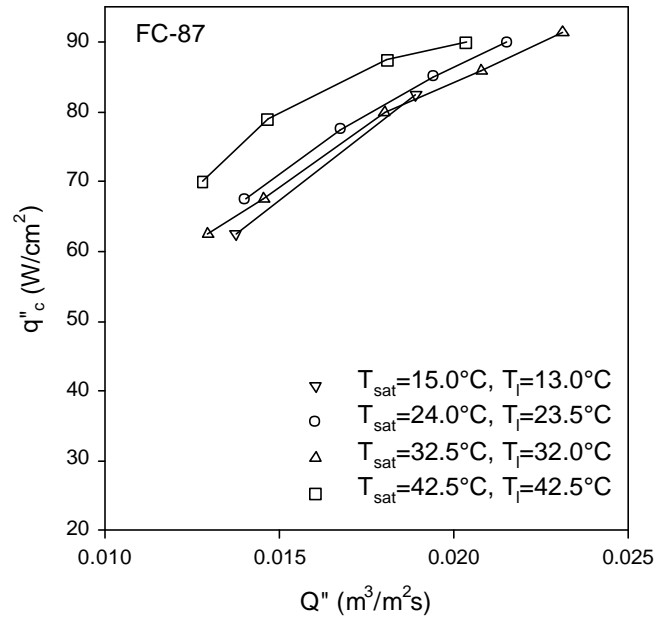


Figure 4.15 CHF vs.  $Q''$  at different saturation temperature levels for FC-87.

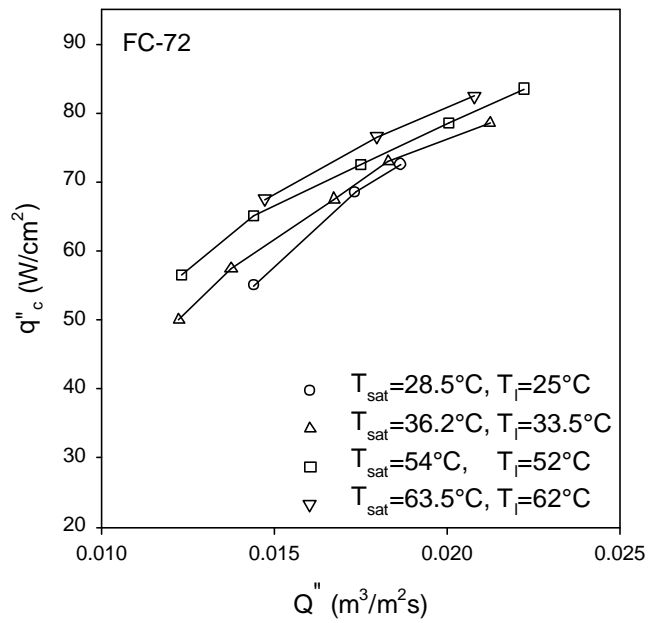


Figure 4.16 CHF vs.  $Q''$  at different saturation temperature levels for FC-72.

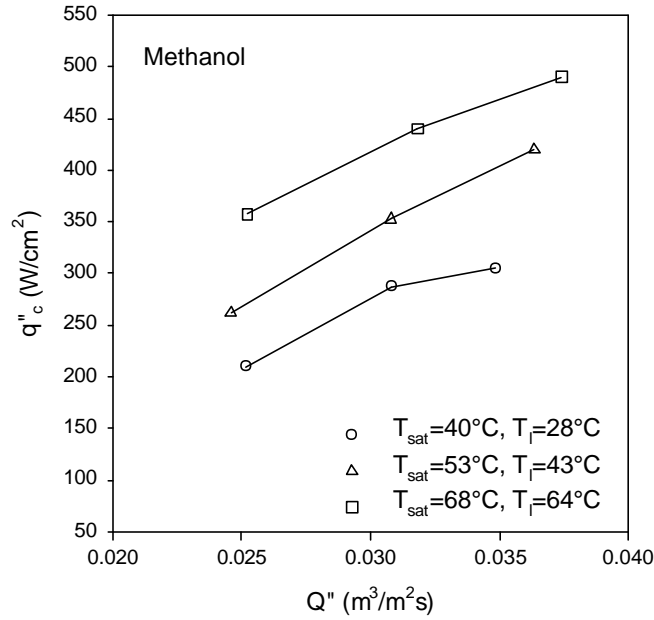


Figure 4.17 CHF vs.  $Q''$  at different saturation temperature levels for methanol.

Some experimental results of CHF are also given in Table 4.1 for comparison. CHF increases with an increase of the volumetric flux or pressure drop because increasing  $Q''$  enhances the momentum of the droplets and the capability of the droplets penetrating through the vapor flow to touch the hot surface. CHF increases with the saturation temperature in the present ranges of tested parameters. For water, the critical heat flux is higher than  $500 \text{ W/cm}^2$ . It has been reported that CHF decreases with the subcooling of the working fluid [19]. The mechanisms of CHF will be discussed in the following section.

#### 4.4 Effect of Noncondensable Gas

The effect of noncondensable gas on the heat transfer of the spray cooling has not been addressed in literature. To discuss the effect of air on the thermal performance of the present spray cooling system, a spray cooling system with a certain amount of air is operated and compared with the system without air. In both cases, FC-72 is used as the working fluid. As the system is idling and not circulating the fluid, the spray chamber pressure is 0.85 bar for the system with the air and 0.295 bar

for the system without air at the same room temperature of 25°C. The relations of  $q''$  with the hot surface temperature,  $T_w$ , for the cases with and without air in the system are plotted in Figure 4.18. The spray chamber outlet temperature,  $T_{ch,o}$ , is used as a parameter shown in Figure 4.18 since it is difficult to determine the spray chamber saturation temperature if the system contains air which can be absorbed and released by FC-72 during its circulation in the closed loop. For comparison, the conditions of the cooling water supply from the cold bath are the same in both systems with and without air involved. The liquid temperature at the inlet of the spray chamber is maintained at 30°C. In the tested parameter ranges, the surface temperature is much lower for the system without air than for the system with the air for a given hot surface heat flux (below CHF). This is because the noncondensable gas causes a higher system pressure,  $p_1$ , as shown in Figure 3.2, and a higher spray chamber pressure which corresponds to a higher saturation temperature. The noncondensable gas increases an overall thermal resistance of the closed loop spray cooling system. At 70 W/cm<sup>2</sup>, the surface temperature is only 72.2°C in the system with pure FC-72 while it is 82.4°C in the system with the air involved. It is believed that the noncondensable gas brings about a higher thermal resistance to the condensation heat transfer in the closed loop system.

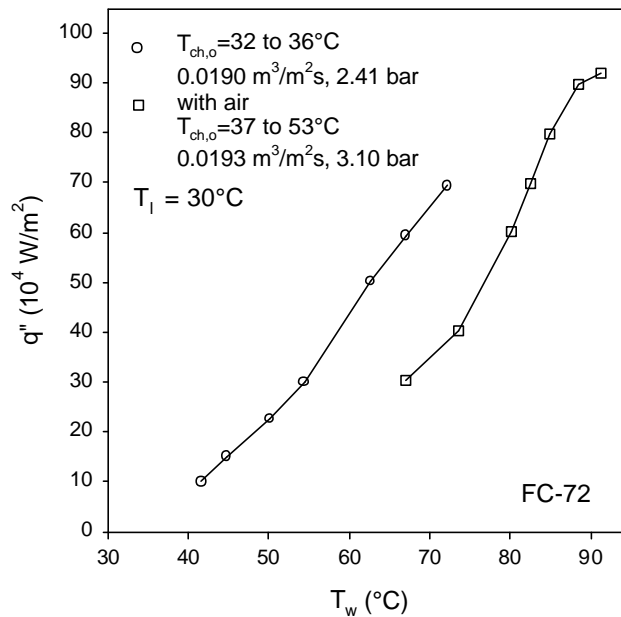


Figure 4.18 Effect of noncondensable gas on the relation between heat flux and hot surface temperature.

Figure 4.19 shows the effect of noncondensable gas on the heat transfer characteristics of the spray over the surface. The data points are plotted as  $q''$  against  $T_w - T_{ch,o}$ . At the heat fluxes lower than  $70 \text{ W/cm}^2$ , the temperature difference of  $T_w - T_{ch,o}$  is lower for the system without air than for the system with the air. This means that the system without air has a better thermal performance of the spray over the surface at  $q'' < 70 \text{ W/cm}^2$ . However, at  $q'' > 70 \text{ W/cm}^2$ , the system with the air provides the smaller values of  $T_w - T_{ch,o}$ , showing a better thermal performance over the surface. This is due to the fact that FC-72 is sprayed along with the air that is released from FC-72 under a reduced pressure in the spray chamber. In this case, a thinner liquid film is produced on the cooling surface because the droplets are smaller in diameter and have higher velocities. Furthermore, the air flow field has increasing ability not only to spread the liquid film but also to sweep away the evaporating vapor and this results in a lower partial vapor pressure in the vicinity of the liquid film surface at the higher pressure drops. The secondary nucleation created by the air is more effective on the spray heat transfer over the hot surface than that by the vapor at the heat fluxes higher than  $70 \text{ W/cm}^2$  in the case of FC-72.

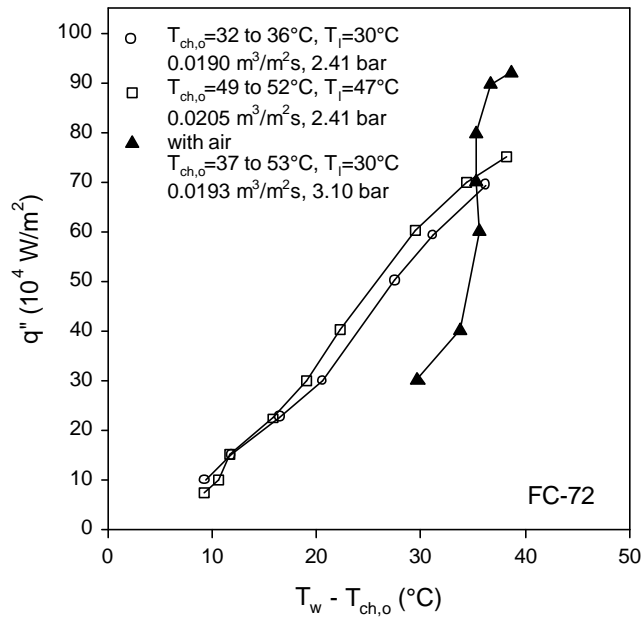


Figure 4.19 Effect of noncondensable gas on heat transfer characteristics over the hot surface.

A comparison of CHF data for the case of pure FC-72 and FC-72 with air is shown in Figure 4.20. The values of CHF for the system with the air involved are higher for the given volumetric flux of  $0.019 \text{ m}^3/\text{m}^2\text{s}$  due to enhanced capability of removing vapor from the hot surface. The subcooling is greater in the system with the air than the system without air if the same power is supplied to the preheater in both cases.

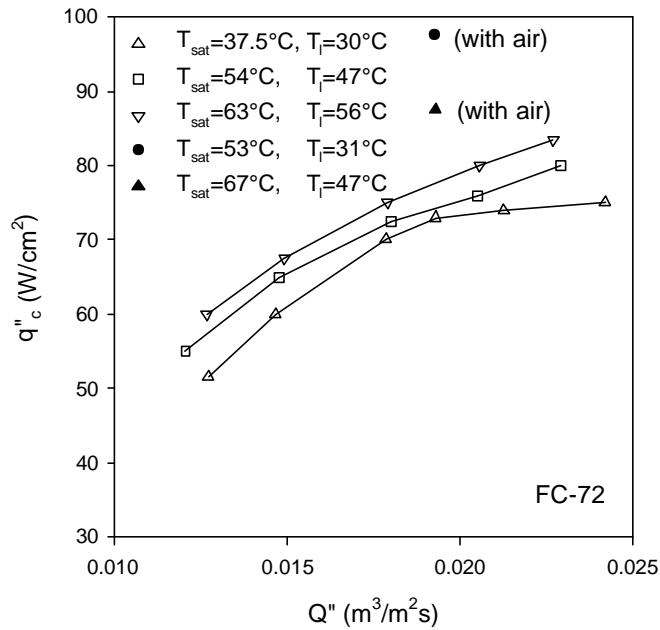


Figure 4.20 Comparison of CHF data for pure FC-72 and FC-72 with air.

## 5 CRITICAL HEAT FLUX CORRELATION

Estes and Mudawar used  $d_{32}$  and  $Q''$  to express the characteristic length and velocity in a general dimensionless CHF correlation [3] and obtained an adequate CHF correlation for spray cooling in a large chamber [5]. Sehmbe et al. developed a semiempirical correlation for CHF and correlated with data of water and LN2 [6]. The correlation was based on macrolayer dryout model which was suggested by Haramura and Katto to deal with CHF in pool and forced convection boiling [20]. In the following, a CHF correlation for multi-nozzle spray cooling is presented from the point of the droplet behavior on the surface.

CHF is caused by the inability of the liquid to reach the hot surface due to the entrainment of the countercurrent vapor flow in local regions and the rebounding and splashing droplets. As the heat flux approaches CHF, discrete vapor layers form on the hot surface and the surface dryout is related with the disappearance of a local liquid film formed by the droplets spreading on the hot surface as shown in Figure 5.1. Increasing the volumetric flux enhances the momentum of the droplets and the capability of the droplets penetrating through the countercurrent vapor flow to touch the hot surface.

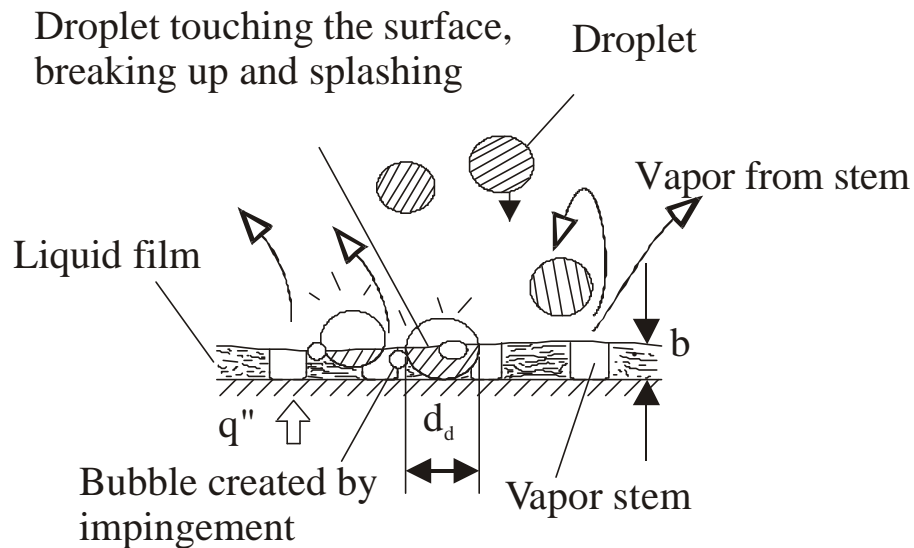


Figure 5.1 Vapor and liquid interaction near CHF.

It is conceivable that prior to the occurrence of CHF, the droplets consecutively hit the surface area covered with preceding droplets,  $(A_w - A_v)$ , where  $A_w$  and  $A_v$  are the cooling surface area and the cross-sectional area of the vapor stem. This means that there are always paths adjacent to the hot surface for vapor to release. At CHF and above CHF, the droplets are unable to touch the surface. It is assumed that upon hitting the surface, the droplet turns into a disc with a diameter of  $d_d$  and a critical thickness of  $b$  and the rest of droplet body rebounds or splashes as shown in Figure 5.1. The critical thickness,  $b$ , is smaller than the average diameter (Sauter mean diameter) of the droplets under the assumption that the droplets should touch the surface as the heat flux is approaching CHF. From this point of view, the heat rate balance on the liquid discs under the dryout condition is written as

$$r_l h_{fg} b (A_w - A_v) N \frac{\rho}{4} d_d^2 = q''_c A_w \quad (6)$$

Eqn. (6) means that the heat rate needed to evaporate the discs on the surface balances the heat rate added to the discs. The liquid disc diameter,  $d_d$ , is assumed to be proportional to the droplet surface mean diameter,  $d_{20}$ , namely,

$$d_d = b d_{20} . \quad (7)$$

The droplet parameters are related as follows:

$$Q'' = N \frac{\rho}{6} d_{20}^2 d_{32} . \quad (8)$$

Now the key point is to determine  $b$ . It is assumed

$$b = a_1 l_H , \quad (9)$$

where  $a_1$  is a constant and  $\lambda_H$  is the Helmholtz critical wavelength given by Eqn. (10) [21]

$$l_H = a_2 \frac{s}{r_v u_v^2} , \quad (10)$$

where  $a_2$  is a constant and the vapor velocity is calculated by

$$u_v = \frac{q''_c}{r_v h_{fg}} \left( \frac{A_w}{A_v} \right) \quad (11)$$

Combining Eqn. (6) with Eqn. (4), and Eqns. (7) to (11), and assuming a constant area ratio of  $A_w/A_v$ , we obtain CHF correlation (12)

$$\frac{q''_c}{r_v h_{fg} Q''} = c We^{-1/3} \left( \frac{r_l}{r_v} \right)^n, \quad (12)$$

where  $c$  is the unknown constant,  $n=0.53$  and  $We$  is the spray Weber number defined as

$$We = \frac{r_l Q''^2 d_{32}}{S}. \quad (13)$$

It is preferred leaving both  $c$  and  $n$  unknown. Using the present CHF data of multi-nozzle spray cooling, the constants of  $c$  and  $n$  in Eqn. (12) are obtained,  $c=0.386$  and  $n=0.549$ , with the standard errors of 0.039 for  $c$ , 0.0154 for  $n$  and 0.937 for the estimate. The final CHF correlation is expressed as

$$\frac{q''_c}{r_v h_{fg} Q''} = 0.386 We^{-1/3} \left( \frac{r_l}{r_v} \right)^{0.549}. \quad (14)$$

The present experimental data and FC-72 data of Estes and Mudawar [5] are compared with Eqn. (14) in Figure 5.2. All of the present data fall within  $\pm 20\%$  of Eqn. (14). The data points of Estes and Mudawar are higher than the correlation by about 33%. The reason could be that the optimum spray distance was selected and air existed in the spray chamber in the test of Estes and Mudawar [5]. It is noted that the scaling parameters in Eqn. (14) are the same as obtained by Estes and Mudawar [5] and Sehmbe et al. [6] though the volumetric flux is estimated in a different way.



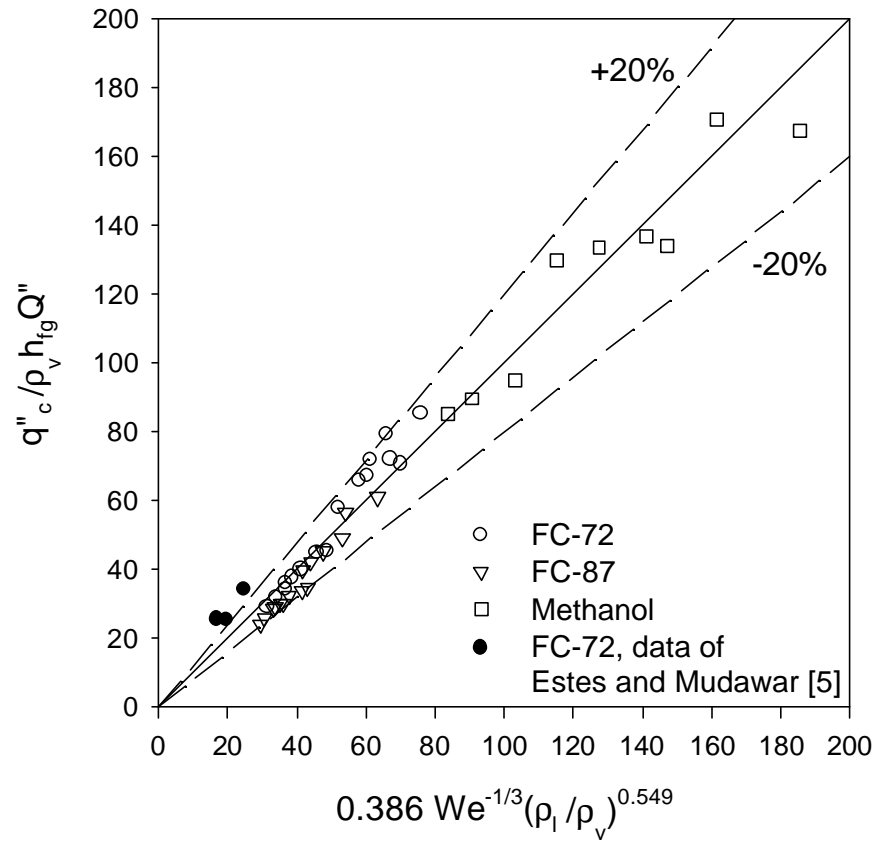


Figure 5.2 Comparison of data with CHF correlation.

## 6 CONCLUSIONS AND RECOMMENDATIONS

### 6.1 Conclusions

A miniature nozzle array with eight miniature nozzles has been designed. A closed loop spray cooling test setup employing the multi-nozzle array is established that can be operated for a pure working fluid test without air in the system and also for the test with a certain amount of air included. The present spray cooling system enables the investigation of the noncondensable gas effect on the heat transfer and CHF of the spray cooling with a fluorocarbon fluid FC-72 as the working fluid. The multi-nozzle spray cooling has been demonstrated in a closed loop system. Heat transfer characteristics and CHF of the spray cooling are experimentally investigated. Accomplishments of the present investigation are summarized as follows.

- ◆ Spray patterns of the eight-nozzle array in the open atmospheric condition are observed using fluorocarbon fluids and water at various liquid supply pressures. It is demonstrated that the nozzles are capable of generating the full cone spray patterns with spray cone angles larger than  $35^\circ$  at the nozzle pressure drops greater than 1.72 bar. In the case of the FC-72 spray at the nozzle pressure drop of 2.76 bar, an average spray cone angle of  $50^\circ$  is obtained.
- ◆ The visual observation of the spray cooling in the confined chamber indicates that nucleate boiling heat transfer takes place in all tested cases and the other two heat transfer modes are convection heat transfer and evaporation from the surface of the liquid film. The interaction between the spray cone and surrounding fluid is stronger in the case of multi-nozzle spray cooling than in the case of single nozzle spray cooling.
- ◆ FC-87, FC-72, methanol and water are used as the working fluids of the closed loop spray system. Data points for the heat transfer and CHF are obtained at various operating temperatures, nozzle pressure drops (from 0.69 bar to 3.10 bar) and heat fluxes. For a given surface superheat, the heat flux increases with the volumetric flux. The pressure drop of 1.72 bar or lower may not be optimum for the maximum heat removal.
- ◆ The closed loop spray cooling can reach the CHF levels up to  $90 \text{ W/cm}^2$  with pure FC-87,  $490 \text{ W/cm}^2$  with pure methanol and greater than  $500 \text{ W/cm}^2$  for pure water. CHF increases with an increase of the volumetric flux or pressure drop.

- ◆ The noncondensable gas adversely affects the overall heat transfer of the closed loop spray cooling system at heat fluxes lower than CHF because of a higher thermal resistance to the condensation heat transfer. The system with pure FC-72 has a better thermal performance of the spray over the surface at  $q'' < 70 \text{ W/cm}^2$ . However, at  $q'' > 70 \text{ W/cm}^2$ , the system containing FC-72 and air shows a better thermal performance over the surface. The presently observed effect of noncondensable gas on the heat transfer and CHF of the spray cooling has not been reported in other prior research publications.
- ◆ Dryout occurs if the droplets are unable to touch the surface. A semiempirical correlation of CHF is presented using the present experimental data for the multi-nozzle spray cooling in the confined and closed system without air involved. All of the present data fall within  $\pm 20\%$  of CHF correlation.

## 6.2 Recommendations

The following recommendations are made for the future research of large area and high heat flux spray cooling.

- ◆ Techniques of fabricating highly integrated multi-nozzle arrays are needed.
- ◆ For large area spray cooling test, an effective removal of the two-phase fluid from the spray chamber will enhance the thermal performance of the spray cooling over the hot surface. An experiment on the large area spray cooling should be conducted.
- ◆ The effect of noncondensable gas on the spray heat transfer could be further investigated by involving various concentrations of the noncondensable gas which could be absorbed by the working fluid.

## 7 REFERENCES

- [1] Yang, J., Chow, L. C., and Pais, M. R., "Nucleate Boiling Heat Transfer in Spray Cooling" Journal of Heat Transfer, Vol. 118, 1996, pp. 668-671.
- [2] Rini, D. P., Chen, R. H., and Chow, L. C., "Bubble Behavior and Nucleate Boiling Heat Transfer in Saturated FC-72 Spray Cooling," Journal of Heat Transfer, Vol. 124, 2002, pp. 63-72.
- [3] Mudawar, I., and Valentine, W. S., "Determination of the Local Quench Curve for Spray-Cooled Metallic Surfaces," Journal of Heat Treating, Vol. 7, No. 2, 1989, pp. 107-121.
- [4] Sehmbe, M. S., Pais, M. R., and Chow, L. C., "Effect of Surface Material Properties and Surface Characteristics in Evaporative Spray Cooling," Journal of Thermophysics and heat Transfer, Vol. 6, No. 3, 1992, pp. 505-512.
- [5] Estes, K. A., and Mudawar, I., "Correlations of Sauter Mean Diameter and Critical Heat Flux for Spray Cooling of Small Surfaces," Int. J. Heat Mass Transfer, Vol. 38, No. 16, 1995, pp. 2985-2996.
- [6] Sehmbe, M. S., Chow, L. C., Hahn, O. J., and Pais, M. R., "Effect of Spray Characteristics on Spray Cooling with Liquid Nitrogen," Journal of Thermophysics and heat Transfer, Vol. 9, No. 4, 1995, pp. 757-765.
- [7] Lin, L., and Ponnappan, R., "Critical Heat Flux of Multi-Nozzle Spray Cooling in a Closed Loop," Paper No. 20073, 37th Intersociety Energy Conversion Engineering Conference, Washington D.C., July 29-31, 2002.
- [8] Keirstead, M., "High Power Diode Lasers," Photonics Spectra, Vol. 34, Issue 1, Laurin Publishing Co., Pittsfield, MA, January 2000.

- [9] Boucke, K., "In Search of the Ultimate Diode Laser," Photonics Spectra, Vol. 35, Issue 9, Laurin Publishing Co., Pittsfield, MA, September 2001.
- [10] Coherent, Inc., Semiconductor Group, "Laser Diode," Fiberoptic Product News, EXFO Electro-Optical Engineering, Inc., September 1999.
- [11] Harnagel, G. L., Vakili, M., Anderson, K. R., Worland, D. P., Endriz, J. G., and Scifres, D. R., "High Power Diode Laser Arrays," IEEE Journal of Quantum Electronics. Vol. 28, 1992, pp. 952-965.
- [12] Point Source, Ltd., "Laser Diode System," Fiberoptic Product News, EXFO Electro-Optical Engineering, Inc., September 1999.
- [13] Brown, C., "Vertical Cavity Nitride System Emits Blue Laser Light," Electronic Engineering Times, CMP Media Inc, Manhasset, NY, October 1999.
- [14] Oh, C. H., Lienhard V, J. H., Younis, H. F., Dahbura, R. S., and Michels, D., "Liquid Jet-Array Cooling Modules for High Heat Fluxes," AIChE Journal, Vol. 44, No. 4, 1998, pp. 769-779.
- [15] Beach, R., Benett, W. J., Freitas, B. L., Munding, D., Comaskey, B. J., Solarz, R. W., and Emanuel, M. A., "Modular Microchannel Cooled Heatsinks for High Average Power Laser Diode Arrays," IEEE Journal of Quantum Electronics. Vol. 28, 1992, pp. 966-976.
- [16] Lin, Y. R., Chung, T. Y., Du, J. H., Chow, L. C., and Bass, M., "Thermal Design in Diode Array Packaging," Paper No. 2002-01-3261, SAE 2002 Power Systems Conference, Coral Springs, FL, Oct. 29-31, 2002.
- [17] Lefebvre, A. H., "Atomization and Spray," Hemisphere, New York, 1989.

- [18] Mudawar, I., and Estes, K. A., "Optimizing and Predicting CHF in Spray Cooling of a Square Surface," *Journal of Heat Transfer*, Vol. 118, 1996, pp. 672-679.
- [19] Tilton, D. E., Pais, M. R., and Chow, L. C., "High Power Density Spray Cooling," WRDC-TR-89-2082, Wright Laboratory, OH, 1989.
- [20] Haramura, Y., and Katto, Y., "A New Hydrodynamic Model of Critical Heat Flux, Applicable Widely to Both Pool and Forced Convection Boiling on Submerged Bodies in Saturated Liquids," *International Journal of Heat and Mass Transfer*, Vol. 26, No. 3, 1983, pp. 389-399.
- [21] Whalley, P. B., "Boiling, Condensation, and Gas-Liquid Flow," *Oxford Engineering Science Series*, Vol. 21, Clarendon Press, New York, 1987.

## APPENDIX A: WORKING FLUID PROPERTIES

(at 25°C unless specified)

### 1. Properties of FC-87

Boiling Point	30°C
Density	1630 kg/m <sup>3</sup>
Vapor pressure	0.813 bar
Specific heat	1.05 kJ/kgK
Thermal conductivity	0.056 W/mK
Viscosity	0.453*10 <sup>-3</sup> kg/ms
Surface tension	0.0095 N/m
Latent heat at boiling point	101.1 kJ/kg

### 2. Properties of FC-72

Boiling Point	56°C
Density	1680 kg/m <sup>3</sup>
Vapor pressure	0.295 bar
Specific heat	1.048 kJ/kgK
Thermal conductivity	0.057 W/mK
Viscosity	0.706*10 <sup>-3</sup> kg/ms
Surface tension	0.012 N/m
Latent heat at boiling point	93.15 kJ/kg

### 3. Properties of Methanol

Boiling Point	65°C
Density	785.5 kg/m <sup>3</sup>
Vapor pressure	0.1593 bar
Specific heat	2.475 kJ/kgK
Thermal conductivity	0.057 W/mK
Viscosity	0.550*10 <sup>-3</sup> kg/ms
Surface tension	0.0222 N/m
Latent heat at boiling point	1183 kJ/kg

### 4. Properties of Water

Boiling Point	100°C
Density	997 kg/m <sup>3</sup>
Vapor pressure	0.0317 bar
Specific heat	4.183 kJ/kgK
Thermal conductivity	0.607 W/mK
Viscosity	0.9*10 <sup>-3</sup> kg/ms
Surface tension	0.072 N/m
Latent heat at boiling point	2442 kJ/kg



## APPENDIX B: MEAN DIAMETERS

Table B.1 Mean diameters and their applications

Symbol	Name of mean diameter	Expression	Application
$d_{10}$	Linear	$\frac{\sum N_i d_i}{\sum N_i}$	Comparisons, evaporation
$d_{20}$	Surface area	$\left[ \frac{\sum N_i d_i^2}{\sum N_i} \right]^{1/2}$	Surface area phenomena, e.g., absorption
$d_{30}$	Volume	$\left[ \frac{\sum N_i d_i^3}{\sum N_i} \right]^{1/3}$	Volume phenomena, e.g., hydrology
$d_{21}$	Surface diameter	$\frac{\sum N_i d_i^2}{\sum N_i d_i}$	Adsorption
$d_{31}$	Volume diameter	$\left[ \frac{\sum N_i d_i^3}{\sum N_i d_i} \right]^{1/2}$	Evaporation, molecular diffusion
$d_{32}$	Sauter mean diameter	$\frac{\sum N_i d_i^3}{\sum N_i d_i^2}$	Mass transfer, reaction
$d_{43}$	DeBrouckere or Herdan	$\frac{\sum N_i d_i^4}{\sum N_i d_i^3}$	Combustion equilibrium
$d_{0.5}$	Mass median diameter		

$d_i$  drop diameter, m

$N_i$  number of drops with  $d_i$  in a spray sample